Title: Delayed localization of A-type lamins to the rupture sites in Hutchinson–Gilford progeria syndrome

Yohei Kono [1, 2, 3], Chan-Gi Pack [4, 5], Takehiko Ichikawa [2], Arata Komatsubara [6], Stephen A. Adam [7], Keisuke Miyazawa [2, 3], Loïc Rolas [8], Sussan Nourshargh [8], Ohad Medalia [9], Robert D. Goldman [7], Takeshi Fukuma [2, 3], Hiroshi Kimura [1, 6], Takeshi Shimi [1, 2*]

Author Affiliation:

[1] Cell Biology Center, Institute of Innovative Research, Tokyo Institute of Technology, Yokohama, Japan.

[2] Nano Life Science Institute (WPI-NanoLSI), Kanazawa University, Kanazawa, Japan.

[3] Faculty of Frontier Engineering, Institute of Science and Engineering, Kanazawa University, Kanazawa, Japan.

[4] Convergence Medicine Research Center, Asan Institute for Life Science, Asan Medical Center, Seoul, Korea.

[5] Department of Biomedical Engineering, University of Ulsan College of Medicine, Seoul, Korea.

[6] School of Life Science and Technology, Tokyo Institute of Technology, Yokohama, Japan.

[7] Department of Cell and Developmental Biology, Feinberg School of Medicine, Northwestern University, Chicago, IL.

[8] Centre for Microvascular Research, William Harvey Research Institute, Faculty of Medicine and Dentistry, Queen Mary University of London, London, UK.

[9] Department of Biochemistry, University of Zurich, Zurich, Switzerland.

The corresponding author:

Takeshi Shimi, Ph.D., Nano Life Science Institute (WPI-NanoLSI), Kanazawa University, Kakuma-machi, Kanazawa, 920-1192, Japan.

Phone: +81-76-234-4540; E-mail: t-shimi@staff.kanazawa-u.ac.jp

Author ORCIDs

Yohei Kono: https://orcid.org/0000-0001-8264-9417

Chan-Gi Pack: https://orcid.org/0000-0002-6578-3099

Takehiko Ichikawa: https://orcid.org/0000-0002-2438-5502

Stephen A. Adam: https://orcid.org/0000-0003-3444-7655

Keisuke Miyazawa: https://orcid.org/0000-0002-5012-8040

Loïc Rolas: https://orcid.org/0000-0001-7617-0768

Sussan Nourshargh: https://orcid.org/0000-0001-5677-1806

Ohad Medalia: https://orcid.org/0000-0003-0994-2937

Robert D. Goldman: http://orcid.org/0000-0003-0383-1435

Takeshi Fukuma: https://orcid.org/0000-0001-8971-6002

Hiroshi Kimura: https://orcid.org/0000-0003-0854-083X

Takeshi Shimi: https://orcid.org/0000-0002-9864-1820

Keywords

Lamin, HGPS, Lamina, Nuclear Envelope Rupture, Nucleus

Abstract

The nuclear lamina (NL) lines the nuclear envelope (NE) to maintain nuclear structure in metazoan cells. The major NL components, the nuclear lamins contribute to the protection against NE rupture induced by mechanical stress. Lamin A (LA) and a short form of the splicing variant lamin C (LC) are diffused from the nucleoplasm to sites of NE rupture in immortalized mouse embryonic fibroblasts (MEFs). LA localization to the rupture sites is significantly slow and weak compared to LC because of its relatively small pool in the nucleoplasm, but the precise mechanism remains unknown. In this study, we induce NE rupture in wild-type and LA/C-knockout MEFs, and Hutchinson–Gilford Progeria syndrome (HGPS) knock-in MEFs that express progerin, a LA mutant lacking the second proteolytic cleavage site, by laser microirradiation and AFM indentation. The farnesylation at the CaaX motif of unprocessed LA and the inhibition of the second proteolytic cleavage decrease the nucleoplasmic pool and slow the localization to the rupture sites in a long-time window (60-70 min) after the induction of NE rupture. Our data could explain the defective repair of NE rupture in HGPS through the farnesylation at the CaaX motif of unprocessed progerin. In addition, unique segments in LA-specific tail region were critical for inhibiting the rapid accumulation within a short-time window (3 min).

Significance Statement

Lamin A (LA) is slowly localized to sites of nuclear envelope (NE) rupture compared to lamin C (LC) because of its relatively small pool in the nucleoplasm. This study reveals that the farnesylation at the CaaX motif of unprocessed LA and the inhibition of the second proteolytic cleavage decreases the nucleoplasmic pool and slows the localization

70 to the rupture sites within a long-time window (60-70 min) after the induction of NE
71 rupture, which may explain the defective repair of NE rupture in Hutchinson–Gilford
72 Progeria syndrome (HGPS). In addition, unique segments in LA-specific tail region
73 cooperate with each other for inhibiting the rapid accumulation within a short-time
74 window (3 min), which is observed with LC.

Introduction

In eukaryotic cell nuclei, the nuclear envelope (NE) spatially separates the nuclear genome from the cytoplasm. The barrier function of the NE is due to two phospholipid bilayers of the inner and outer nuclear membranes (INM, ONM). The INM is in contact with chromatin at the nuclear side via INM proteins (1), whereas the ONM is connected with the cytoskeletal system through the linker of nucleoskeleton and cytoskeleton (LINC) complex (2), and is continuous with membranous organelles including the endoplasmic reticulum (ER) (3). The nuclear lamina (NL) is closely apposed to the INM and associates with heterochromatin to support nuclear structure. Nuclear pore complexes (NPCs) fill holes formed by the INM-ONM fusion for nucleo-cytoplasmic transport and interact with euchromatin (4).

The NL structure consists of the nuclear lamins and associated proteins (5). The lamins are type V intermediate filament proteins, which are subdivided into A-type lamins (lamins A [LA] and C [LC]) and B-type lamins (lamins B1 [LB1] and B2 [LB2]) (6, 7). LA and LC are derived from the single gene *LMNA* by alternative splicing (8), whereas LB1 and LB2 are encoded by separate genes *LMNB1* and *LMNB2*, respectively (9-12). Lamin molecules assemble into a filament with a diameter of ~3.5 nm and these filaments appear to non-randomly lay on top of each other to form meshworks of the NL with a thickness of ~13.5 nm in immortalized mouse embryonic fibroblasts (MEFs) (13, 14). LA/C and LB1 filaments associate with the outer ring structure of the NPC and are involved in regulating the distribution of the meshworks and NPCs (13-16).

The −CaaX box at the C terminus of unprocessed LA, LB1 and LB2 (pre-LA, pre-LB1 and pre-LB2, respectively) is post-translationally processed in steps, including the attachment of farnesyl group to the cysteine residue of the −CaaX box by a

99 farnesyltransferase (17, 18), proteolytic cleavage of three residues (−aaX) by an aaX
100 endopeptidase (19) and carboxyl methylation of the terminal carboxylic acid group
101 (−COOH) of the C-terminal cysteine residue by a carboxyl methyltransferase (20). The
102 maturation of LB1 and LB2 is completed by these steps. In case of the farnesylated and
103 carboxymethylated pre-LA, an additional 15 C-terminal residues including the
104 farnesylated and carboxymethylated cysteine, are cleaved off by Zinc metallopeptidase
105 STE24 (Zmpste24/FACE1) to produce the mature form (mature-LA) (21, 22).

106 The NE is locally ruptured during physiological and pathological circumstances.
107 Immediately after NE rupture, NE components are recruited to the rupture sites with the
108 endosomal sorting complex required for transport-III (ESCRT-III) complex and barrier-
109 to-autointegration factor (BAF) (23-25). Nuclear DNA adjacent to the rupture sites is
110 recognized by the DNA sensors cyclic GMP-AMP synthase (cGAS) and its downstream
111 signaling effector STING (23-25). The frequencies of spontaneous and forced NE rupture
112 are significantly increased by the depletion of lamins (26-29). LA/C promotes the
113 accumulation of BAF and cGAS at the rupture sites (30). Numerous mutations that have
114 been found throughout the *LMNA* gene cause a spectrum of human genetic disorders,
115 collectively called laminopathies (31). Laminopathies associated with dilated
116 cardiomyopathy (DCM), muscular dystrophy (MD), familial partial lipodystrophy
117 (FPLD) and Hutchinson–Gilford Progeria syndrome (HGPS) are frequently accompanied
118 by spontaneous NE rupture (32-34). In HGPS, the heterozygous transversion of a
119 nucleotide substitution at position 1824 T>C (G608G) leads to abnormal splicing of the
120 last 150 nucleotides of exon 11, resulting in the production of unprocessed HGPS mutant,
121 progerin (PG) (pre-PG) which lacks 50 amino acids (residues 607–656) from the C
122 terminus of pre-LA (Fig. 1 A). Because these residues contain the second proteolytic

123 cleavage site involved in pre-LA processing, the mature form (mature-PG) remains
124 farnesylated and carboxymethylated, leading to its permanent association with the INM
125 (35, 36).

126 Previous studies demonstrate that LA/C is recruited to the rupture sites with BAF
127 (30, 37, 38) but LA is significantly slow and weak in localizing to the rupture sites
128 compared to LC (30, 39, 40) because it is less abundant in the nucleoplasm than LC (30,
129 39, 40). However, a molecular mechanism for retaining nucleoplasmic LA sparse and
130 slowing its localization to the rupture sites still remains to be elucidated. Here, we
131 investigate the role of the C-terminal tail region specific for LA in this mechanism. We
132 previously showed that mEmerald-fused LA accumulated at the rupture sites only when
133 it was overexpressed at a high level (30), and the accumulation kinetics appeared to be
134 artifactual because it was not confirmed with endogenous LA detected by
135 immunofluorescence (30). Therefore, we establish the ectopic expression system for live-
136 cell imaging and fluorescence correlation spectroscopy (FCS) to express mEmerald-fused
137 LA, alternate forms of LA, and LC at a low level with the endogenous promotor in wild
138 type (WT), HGPS and LA/C-knockout (KO) MEFs. Our data reveal the significance of
139 the LA-specific tail region for retaining its small pool in the nucleoplasm and slowing its
140 localization to the rupture sites.

141 ## Results

142 **PG is not only slow in localizing to the rupture sites but also slows LA localization**

143 To investigate the involvement of the pre-LA processing in retaining small pool of LA in
144 the nucleoplasm and slowing its localization to the rupture sites, we used immortalized
145 WT MEFs and heterozygous knock-in MEFs with PG expression from a mutant allele of
146 the *Lmna* gene carrying the c.1827C>T; p.Gly609Gly mutation (*Lmna*$^{G609G/+}$, G609G/+).
147 This mutation is equivalent to the HGPS mutation in the human *LMNA* gene (41, 42).
148 These cells stably expressed super-folder Cherry harboring two NLSs derived from SV40
149 large T antigen and c-Myc (NLS-sfCherry) as a NE rupture marker (30). Because
150 spontaneous NE rupture is frequently observed in skin fibroblasts derived from a HGPS
151 patient and mouse smooth muscle cells (SMCs) expressing PG (32, 34), we first examined
152 if G609G/+ MEFs also exhibit misshapen nuclei, the leakage of NLS-sfCherry to the
153 cytoplasm, the mis-localization or decreased expression of LB1, and the local
154 accumulation of cGAS, which are all indicative of spontaneous NE rupture. WT and
155 G609G/+ cells were stained with Hoechst 33342 for DNA and specific antibodies directed
156 against LB1 and cGAS (Fig. S1 A). Unlike the HGPS patient cells and PG-expressing
157 mouse SMCs, G609G/+ cells did not show these phenotypes compared to WT cells (Table
158 S1), indicating that the HGPS mutation is not accompanied by spontaneous NE rupture
159 in these cells. Next, to examine the effect of this mutation on recovery from forced NE
160 rupture, single-cell compression by AFM indentation was applied to these cells, and the
161 nuclear reentry of NLS-sfCherry was observed by time-lapse imaging before and after
162 the induction of the rupture (Fig. 1 B) (43). Interestingly, G609G/+ cells showed a
163 significantly slow reentry compared to the WT cells which had a ~50% recovery from the

164 original fluorescence intensity ~4 min after the induction of NE rupture (Fig. 1 C and D),
165 indicating that PG expression slows the recovery from forced NE rupture.

166 To determine the localization kinetics of LA and PG at the rupture sites within a
167 relatively long-time window, WT and G609G/+ cells were fixed at 0-10, 30-40, 60-70
168 and 120-130 min after the induction of NE rupture by 405-nm laser microirradiation (Fig.
169 1 E) (30), and then stained with Hoechst 33342 for DNA and the specific antibodies
170 directed against LA and PG which do not cross-react to each other (Fig. 1 A). At 0-10,
171 30-40, 60-70 and 120-130 min after the rupture, LA was localized to the rupture sites in
172 ~4%, ~55%, ~77% and ~86% of WT nuclei and ~8%, ~29%, ~61% and ~68% of
173 G609G/+ nuclei, respectively (Fig. 1 F, G and Fig. S1 B), whereas PG was slower in
174 localizing to the rupture sites of G609G/+ nuclei than LA, showing ~0%, ~7%, ~32% and
175 ~50%, respectively (Fig. 1 F, G and Fig. S1 B). These results suggest that PG expression
176 decelerates the localization kinetics of LA at the later time points (60 and 120 min). In
177 addition, both LA and PG are likely to be recruited to the rupture sites with BAF within
178 a relatively long-time window according to our results from BAF knockdown (KD)
179 experiments with short hairpin RNAs (shRNAs) (Fig. S1 C-E). WT cells expressing a
180 shRNA for the control (Scramble) or two shRNAs (shBAF #1 and #2) were fixed at 60-
181 70 min after the induction of NE rupture by laser microirradiation, and then LA
182 localization was determined by immunofluorescence. As expected, LA was localized to
183 the rupture sites in ~61%, 10% and ~16% of the control and BAF-KD#1 and #2 nuclei,
184 respectively (Fig. S1 D and E), indicating that BAF is required for LA localization to the
185 rupture sites. These results are similar to a previous finding to indicate that BAF rapidly
186 recruits overexpressed GFP-LA to the rupture sites (37).
187

188 **PG slows LC accumulation to the rupture sites**

189 Because the accumulation of LC to the rupture sites was much earlier (within 3 min) than
190 the localization of LA or PG (30-120 min) (30, 39, 40) (Fig. 1 F and G) and LC depletion
191 accelerates the cytoplasmic leakage of NLS-sfCherry at the early time points (within 10
192 min) (30), LC might be directly linked to the delay in retrieving NLS-sfCherry from the
193 cytoplasm of G609G/+ cells within 10 min after the induction of forced NE rupture (Fig.
194 1 C and D). Therefore, PG expression could slow LC accumulation to the rupture sites.
195 To test this idea, endogenous LA, LC and PG were directly labeled with a LA/C-specific
196 genetically encoded probe, designed ankyrin repeat protein (DARPin)-LaA_6 (44), fused
197 with super-folder GFP (sfGFP), sfGFP-DARPin-LA6 in WT and G609G/+ cells
198 expressing NLS-sfCherry (30) (Fig. S2 A). Then, live-cell imaging was carried out before
199 and after the induction of NE rupture by laser microirradiation. Because endogenous LA
200 and PG did not localize to the rupture sites within 3 min after the induction of NE rupture
201 (30) (Fig. 1 G), sfGFP-DARPin-LA6 accumulating at the rupture sites only represented
202 endogenous LC within such a short-time window. Immediately after the induction of NE
203 rupture, the accumulation of sfGFP-DARPin-LA6 was significantly weaker in G609G/+
204 nuclei compared to WT nuclei (Fig. S2 B and C), indicating that PG expression attenuates
205 LC accumulation.

206

207 **PG slows the diffusion of LC in the nucleoplasm**

208 Because of the slow recruitment of LC from the nucleoplasm to the rupture sites in
209 G609G/+ nuclei (Fig. S2 B and C), the diffusion fractions and coefficients in the
210 nucleoplasm could be decreased in G609G/+ nuclei compared to WT nuclei. To determine
211 them, mEmerald-LC was stably expressed at a low level from the *Rosa26* locus under the

212 endogenous *Lmna* promotor in WT and G609G/+ cells, and fluorescence correlation
213 spectroscopy (FCS) was performed using these cells (Fig. S3 A-D). The auto-correlation
214 curve obtained by the signal detection was fitted with fast and slow components (15, 45,
215 46). Interestingly, the diffusion coefficients of fast components were significantly high in
216 WT nuclei compared to G609G/+ nuclei (Fig. S3 D). This result indicates that PG
217 expression significantly decreases the diffusion coefficient of fast component despite the
218 increased fraction but this degree of difference is insufficient for explaining the weak
219 accumulation of sfGFP-DARPin-LA6 at the rupture sites in G609G/+ nuclei compared
220 to WT nuclei.
221

222 **The nucleoplasmic pools of LA and PG are increased by the inhibition of**
223 **farnesylation**

224 When the CaaX motifs of pre-LA and pre-PG are farnesylated (18, 36, 47), they are
225 retained at the NE through the hydrophobic interaction with the lipid bilayer of the INM
226 (47, 48). Therefore, the inhibition of farnesylation with FTI could increase their
227 nucleoplasmic pools, leading to their fast localization to the rupture sites. To test this
228 possibility, WT and G609G/+ cells were treated with DMSO for the control or
229 farnesyltransferase inhibitor (FTI), 3.2 μM lonafarnib for 48 h, and the expression levels
230 and localization of LA and PG were determined by immunoblotting using the specific
231 antibodies directed against LA/C, and by immunofluorescence using the LA and PG
232 antibodies respectively, (Fig. 2 A). For immunoblotting, pre-LA, mature-LA, pre-PG,
233 mature-PG, and LC were detected with the antibodies directed against LA/C (for all) and
234 PG (for pre- and mature-PG). For immunofluorescence, the LA antibody (for pre- and
235 mature-LA) and the PG antibody (for pre- and mature-PG) were used. As expected, the

236 levels of pre-LA and pre-PG were increased in FTI-treated cells compared to the control
237 cells as shown as the upper and lower band of LA and PG (Fig. 2 A). Based on ratios of
238 the average fluorescence intensity in the nucleoplasmic pool relative to that of the NL
239 (NP/NL ratios), LA and PG were significantly abundant in the nucleoplasm of FTI-treated
240 nuclei compared to the control nuclei (Fig. 2 B and C), indicating that LA and PG are
241 increased in the nucleoplasmic pool by FTI treatment. Next, these cells were fixed within
242 10 min and at 60-70 min after the induction of NE rupture by laser microirradiation, and
243 the localization of LA and PG to the rupture sites was detected by immunofluorescence.
244 LA was localized to the rupture sites within 10 min in ~7% and ~7% of WT and G609G/+
245 nuclei for the control and ~18% and ~17% of WT and G609G/+ nuclei treated with FTI,
246 respectively, and PG in 0% and ~37% of the control and FTI-treated G609G/+ nuclei,
247 respectively (Fig. S4). At 60-70 min, LA localization to the rupture sites was observed in
248 ~59% and ~42% of the control nuclei and ~91% and ~74% of FTI-treated WT and
249 G609G/+ nuclei, respectively, and PG localization in ~18% and ~81% of the control and
250 FTI-treated G609G/+ nuclei, respectively (Fig. 2 D). These results indicate that the
251 inhibition of farnesylation promotes the localization of LA and PG to the rupture sites.
252

253 **PG becomes diffusible in the nucleoplasm by FTI treatment**

254 Because of the increases in nucleoplasmic pool of LA and PG by FTI treatment
255 (Fig. 2 B and C), the non-farnesylated forms could be highly mobile in the nucleoplasm
256 of FTI-treated cells. To test this idea, the diffusion coefficients of mEmerald-LA and PG
257 were measured by FCS (Fig. 3 A). For the FCS measurements, mEmerald-LA and PG
258 were stably expressed at a low level by the same system as described above with
259 mEmerald-LC (Fig. S3 A and B), followed by the treatment with DMSO for the control

260 or FTI (Fig. S4). The diffusion fractions of mEmerald-LA in the control and FTI-treated
261 WT and G609G/+ nuclei were all similar to each other (Fig. 3 B and C) but the diffusion
262 coefficient of fast component was slightly but significantly small in G609G/+ nuclei
263 compared to WT nuclei whereas that of slow component remained unchanged (Fig. 3 C).
264 These results show that PG expression slows the diffusion speed of mEmerald-LA. On
265 the other hand, the diffusion signals of mEmerald-PG were barely detectable in the
266 nucleoplasm of WT and G609G/+ nuclei for the control. Instead, the signal decays caused
267 by photobleaching were observed during the FCS measurements (Fig. 3 D), strongly
268 suggesting that these signals originate from the NL where mEmerald-PG are immobile
269 (15, 53). When WT and G609G/+ cells were treated with FTI, the diffusion signals were
270 detected by FCS as expected (Fig. 3 D and E), indicating that PG becomes diffusible in
271 the nucleoplasm by FTI treatment. Therefore, the nucleoplasmic pool is the likely source
272 of PG localized to the rupture sites (Fig. 2 C and D).
273

274 **The second proteolytic cleavage is required for the localization of LA to the rupture**
275 **sites**

276 The localization of PG to the rupture sites was significantly slow compared to LA (Fig. 1
277 G), and the permanent association of PG with the INM due to the absence of the second
278 proteolytic cleavage site could decelerate the localization kinetics (35, 36). To check this
279 possibility, Zmpste24, which endoproteolytically processes both the CaaX motif and the
280 second cleavage site (54) was knocked down by shRNAs in WT MEFs, and then the
281 expression levels and localization of pre- and mature-LA were determined in cells
282 expressing shRNAs for the control or Zmpste24 KD by immunoblotting and
283 immunofluorescence, respectively (Fig. S5 A). A specific antibody directed against pre-

284 LA used for immunoblotting and immunofluorescence reacts with pre-LA but not mature-
285 LA (Fig. 1 A). The C-terminal residues of pre-LA including the CaaX motif remained
286 partially uncleaved by Zmpste24 KD, resulting in the significant increase and decrease in
287 expression level of pre- and mature-LA, as shown as the upper and lower band,
288 respectively (Fig. S5 A). These results are consistent with the previous findings to indicate
289 that Zmpste24 KD inhibits the second cleavage (55). LA and pre-LA were predominantly
290 localized to the NL, and the NP/NL ratios remained unchanged in Zmpste24-KD cells
291 compared to the control cells (Fig. S5 B and C). These cells were fixed at 60-70 min after
292 the induction of NE rupture by laser microirradiation, and then the localization of LA and
293 pre-LA to the rupture sites was determined by immunofluorescence. LA was localized at
294 the rupture sites in ~75% of the control cells whereas LA and pre-LA were completely
295 absent from the rupture sites in Zmpste24-KD cells (Fig. S5 D and E), indicating that the
296 second cleavage is required for their localization to the rupture sites.
297

298 **Inhibition of farnesylation at the CaaX motif is sufficient for the localization of LA**
299 **to the rupture sites without the second proteolytic cleavage**

300 Zmpste24 depletion significantly increased the pre-LA expression level (56) (Fig. S5 A
301 and B), which is accompanied by the farnesylation at the CaaX motif (49). Therefore, the
302 inhibition of the farnesylation with FTI could release the pre-LA from the NE, resulting
303 in the fast localization of pre-LA to the rupture sites. To test this idea, the control
304 (Scramble) and Zmpste24-KD cells were treated with DMSO or FTI as before, and the
305 expression levels and localization of pre- and mature-LA were determined by
306 immunoblotting and immunofluorescence, respectively (Fig. 4 A and B). As expected,
307 Zmpste24 KD increased and decreased the pre- and mature-LA levels, respectively in

308 DMSO- and FTI-treated cells (Fig. 4 A). FTI treatment also had the similar effect in the
309 control cells but the synergetic effect with Zmpste24 KD was very subtle (Fig. 4 A). To
310 analyze the localization of pre- and mature-LA in those cells by immunofluorescence,
311 specific antibodies directed against them that do not cross-react with each other were used.
312 In the control cells treated with DMSO, pre-LA was under the detection limit whereas
313 mature-LA was predominantly localized to the NL (Fig. 4 B-D). When the control cells
314 were treated with FTI, pre-LA became clearly visible in the NL and mature-LA was less
315 prominent there instead (Fig. 4 B-D). In Zmpste24-KD cells treated with DMSO, pre-LA
316 was localized to the NL and mature-LA was undetectable (Fig. 4 B-D). FTI treatment
317 decreased pre-LA localization to the NL up to the level of the control cells treated with
318 FTI and mature-LA was undetectable (Fig. 4 B-D). These results were consistent with the
319 known effect of FTI treatment, which inhibit the farnesylation at the CaaX motif and the
320 following processes including the second cleavage, leading to release the pre-LA from
321 the NE (50). As FTI treatment increases nucleoplasmic LA levels regardless of the second
322 cleavage, we hypothesize that LA localizes to the rupture site more efficiently in FTI. The
323 localization of pre- and mature-LA to the rupture sites was determined in these cells by
324 immunofluorescence at 60-70 min after the induction of NE rupture by laser
325 microirradiation. Pre-LA was localized to the rupture sites in ~97%, ~12% and ~77% of
326 FTI-treated control, DMSO- and FTI-treated Zmpste24-KD nuclei, respectively (Fig. 4
327 E). This indicates that pre-LA without farnesylation present in the nucleoplasm
328 effectively localizes to the rupture sites, supporting the hypothesis. However, the
329 localization of mature-LA was slightly decreased in the control cells by FTI treatment
330 (Fig. 4 E), despite FTI treatment increases the localization of pre- and mature-LA using

331 antibody directed against both (Fig. 2 D), probably because its nucleoplasmic level was
332 not as high as pre-LA (Fig. 2 C, 4 C and D).
333
334 **LA differs from LC in localization to the rupture sites through two specific**
335 **sequences in the tail region**
336 The inhibition of farnesylation at the CaaX motif of PG significantly increased the
337 nucleoplasmic pool and promoted the localization to the rupture sites within 10 min after
338 the induction of NE rupture (Fig. S4). Interestingly, PG was not localized to the rupture
339 sites within the first half of the time window (0-5 min) whereas LC rapidly accumulated
340 (30) (Fig. S2). Therefore, we confirmed the effect of this inhibition on their NP/NL ratios
341 and the accumulation kinetics at the rupture sites within the short-time window (3 min)
342 by live-cell imaging using mEmerald-fused LA-full length (FL), LC, PG and the non-
343 farnesylated mutant of PG, PG-CSM that lacks the isoleucine within the CaaX motif were
344 expressed in LA/C-KO MEFs (Fig. 5 A). As expected, the NP/NL ratio of mEmerald-PG
345 was similar to that of mEmerald-LA-FL, whereas that of mEmerald-PG-CSM was
346 significantly high but not to the extent of mEmerald-LC (Fig. 5 B and C). mEmerald-PG
347 and mEmerald-PG-CSM did not accumulate at the rupture sites (Fig. 5 D), indicating that
348 the inhibition of the farnesylation is not sufficient for exhibiting the rapid accumulation
349 that was similar to that of mEmerald-LC. These results strongly suggest that the tail
350 regions specific for LA and PG are involved in inhibiting the rapid accumulation. In
351 human and mice, LC harbors identical six amino acids whereas LA has 98 and 97 amino
352 acids, following the residues 1-566 and 1-568 shared between LA and LC, respectively
353 (Fig. S6 A). Because this LC-specific amino acids do not contribute to the rapid
354 accumulation at the rupture sites (30), mEmerald-fusion proteins of LA truncation

355 mutants, LA-S575X, LA-A601X, LA-S617X, LA-F627X, LA-T644X and LA-L648X
356 were tested for their NP/NL ratios and the accumulation kinetics within 3 min (Fig. 5 A).
357 Among these mutants, mEmerald-LA-S575X has the highest NP/NL ratio (Fig. 5 B and
358 C), and only this mutant rapidly accumulated within 3 min (Fig. 5 D and S6 B), indicating
359 that the residues 575-600 is involved in inhibiting the rapid accumulation. Because the
360 deletion mutant, mEmerald-LAΔ26 did not accumulate at the rupture sites (Fig. 5 D),
361 further truncation was performed at the C-terminal side of mEmerald-LAΔ26 to produce
362 mEmerald-LAΔ26-L627X, mEmerald-LAΔ26-L644X and mEmerald-LAΔ26-L648X
363 (Fig. 5 A). The NP/NL ratio remained unchanged by these truncations compared to
364 mEmerald-LAΔ26 (Fig. S6 C and D) but only mEmerald-LAΔ26-L627X rapidly
365 accumulated (Fig. 5 E and S6 E). These results show that the residues 627-643 assists
366 LAΔ26 to inhibit the rapid accumulation without decreasing the nucleoplasmic pool. We
367 therefore designated the residues 575-600 as LA-characteristic sequence-1 (LACS1) and
368 the residues 627-643 as LACS2.

369 **Discussion**

370 A-type lamins are localized to sites of NE rupture for the repair (23, 24, 30). Our previous
371 study shows that endogenous LC but not LA rapidly accumulates the rupture sites within
372 3 min after the induction of NE rupture because LC is more abundant in the nucleoplasm
373 than LA (30, 39, 40). LA can rapidly accumulate only when LA is overexpressed at a high
374 level to increase the nucleoplasmic pool (30, 37, 38). LC accumulation requires both the
375 immunoglobulin-like fold (Ig-fold) domain that binds to BAF and a nuclear localization
376 signal (NLS), and is not attributable to the LC-specific amino acids (30). In this study, we
377 analyze the LA-specific tail region to determine a molecular mechanism for retaining its
378 small pool in the nucleoplasm and decelerating localization kinetics at the rupture sites,
379 and Fig. 6 illustrates our current findings following our previous study (30). The
380 proteolytic removal of 15 amino acids containing the farnesylated C-terminal end of pre-
381 LA by Zmpste24 increases the nucleoplasmic pool and accelerates the localization
382 kinetics at the rupture sites within the long-time window (60-70 min) after the induction
383 of NE rupture. In HGPS, pre-PG lacks 50 amino acids containing the second proteolytic
384 cleavage site from the C terminus of pre-LA, leading to the permanent association with
385 the INM, which significantly decreases the nucleoplasmic pool and decelerates the
386 localization kinetics at the rupture sites. In contrast, FTI treatment pronouncedly increases
387 the nucleoplasmic pools of LA and PG and promotes their localization to the rupture sites.
388 Therefore, the processes for increasing the nucleoplasmic pool is likely to be rate-limiting
389 steps for the localization kinetics within this time window. Additionally, LACS1
390 cooperates with LACS2 to inhibit the rapid accumulation at the rupture sites within the
391 short-time window (3 min).

392 We use immortalized WT and G609G/+ MEFs to analyze the NP/NL ratios of

393 LA, pre-LA and PG, and their localization kinetics at the rupture sites. Unlike HGPS-
394 patient cells and mouse SMCs expressing PG (32, 34, 58), our G609G/+ cells do not
395 exhibit the formation of misshapen nuclei and spontaneous NE rupture, which could be
396 due to the immortalization process with SV40 large T antigen. In oncogene-induced
397 senescence of normal human fibroblasts, DNA protrusion from the nucleus, micronuclei
398 formation and the leakage of nuclear contents are coupled to the loss of LB1 (59-61). The
399 LB1 expression level could also decrease when HGPS-patient cells become prematurely
400 senescent (62) and PG expression levels increase with age in aortas from G609G/+ mice
401 whereas LB1 levels decrease (34). Therefore, spontaneous NE rupture might be induced
402 by the HGPS mutation because of the induction of premature senescence and rapid
403 cellular aging.

404 Instead of spontaneous NE rupture, we find that upon the induction of forced NE
405 rupture by AFM indentation, the nuclear reentry of NLS-sfCherry is significantly slow in
406 G609G/+ cells compared to WT cells, strongly suggesting that a repair process of forced
407 NE rupture is impaired by PG expression. The LA expression level in G609G/+ cells is
408 reduced compared to that in WT cells due to the efficient alternative splicing from the
409 mutant allele of the *Lmna* gene (41, 63), which could explain its smaller pool in the
410 nucleoplasm compared to WT cells to decelerate the localization kinetics at the rupture
411 sites. On the other hand, the LC expression level could be increased in G609G/+ cells
412 compared to WT cells for some reason (40, 41). However, the diffusion of the fast
413 component is significantly slow in the nucleoplasm of G609G/+ nuclei compared to WT
414 nuclei, as our results indicate. This could be explained if there is a possibility that LC is
415 increased in the NL and decreased in the nucleoplasm because of the strong association
416 with the NL by PG expression. To support this idea, LC has a significantly slow turnover

417 in the NL of HGPS-patient nuclei compared to normal nuclei (53, 64). These results
418 suggest that the alteration in expression and distribution of LA/C by PG expression impair
419 the repair of NE rupture.

420 We find that when the farnesylation at the CaaX motif of pre-LA and pre-PG is
421 inhibited by FTI treatment, they are increased and become diffusible in the nucleoplasm
422 to accelerate the localization kinetics to the rupture sites, indicating that the farnesylation
423 process limits the localization to the rupture sites regardless of the second cleavage of
424 pre-LA. Furthermore, Zmpste24 KD blocks the second cleavage, leading to the complete
425 inhibition of pre-LA localization to the rupture sites, and the effects of Zmpste24 KD on
426 the NP/NL ratios and the localization kinetics are rescued by FTI treatment. These results
427 strongly suggest that pre-LA is mostly farnesylated in Zmpste24 KD cells and that the
428 nucleoplasmic pool is little or none to localize to the rupture sites within 60 min.

429 Apart from the farnesylation at the CaaX motif and the inhibition of the second
430 cleavage of pre-LA, we find that LACS1 and LACS2 in the tail region are also involved
431 in slowing the localization to the rupture sites. Because the truncation of LACS1
432 significantly increases the NP/NL ratios, LA appears to be retained at the NL through
433 LACS1 compared to LC, resulting in the slow localization. It is possible that LACS1
434 contributes to the formation of lamin filaments in the NL and/or interacting with other
435 NE components including INM proteins. On the other hand, LACS2 could assist the
436 LACS1 function for inhibiting LA localization to the rupture sites without promoting the
437 retention of LA at the NL. Because the truncation of the residues 599-625 between
438 LACS1 and LACS2 in human increases the NP/NL ratios, a segment within these amino
439 acids is likely to retain its small pool in the nucleoplasm. Whereas the residues 411-553
440 including the NLS and the Ig-fold domain interacts with dsDNAs (67), the residues 506-

441 638 binds histone H3 (68). This chromatin-binding domain contains the LACSs,
442 suggesting that LA is partially tethered to chromatin through LACSs to slow the
443 localization to the rupture sites.

444 In HGPS, the permanent association of PG with the INM by the farnesylation at
445 the CaaX motif significantly reduces the nucleoplasmic pool, leading to the slow
446 localization to the rupture sites. Similarly, this mechanism could be also critical for their
447 accesses to active enhancers in the nuclear interior to affect the gene expression in HGPS
448 patient cells (69). Other studies show that the PG association with the INM can lead to
449 the increased NE instability (32, 34) but we do not observe spontaneous NE rupture in
450 our G609G/+ cells. Nevertheless, our findings of the slow localization kinetics of LA, LC
451 and PG at the rupture sites implicate pathological significance of the defective repair of
452 the NL. The therapeutic effect of FTI treatment appears to rescue from the repair defect
453 by targeting the farnesylation of PG. Therefore, the induction of spontaneous NE rupture
454 and the rescuing with FTI treatment need validating using the mouse model of HGPS in
455 future studies.

456 ## Materials and methods

457 **Plasmid construction**

458 Two different NLSs derived from SV40 large T antigen (NLS^{SV40}; PKKKRKV) and c-
459 Myc (NLS^{Myc}; PAAKRVKLD) from pCDH-NLS^{SV40}-sfCherry-NLS^{Myc}-Blast (30) were
460 ligated to pCDH-CMV-MCS-EF1-Hygro (plasmid #CD515B-1, System Biosciences)
461 using the Ligation-Convenience Kit (Nippon Gene) and designated as pCDH-NLS^{SV40}-
462 sfCherry-NLS^{Myc}-Hygro. The annealed oligonucleotides to express shRNAs (Zmpste24,
463 TRCN0000366641; BAF#1, TRCN0000124958; BAF#2, TRCN0000124955; Table S2,
464 Broad Institute) were ligated into pLKO.3-blast (30) using the Ligation-Convenience Kit.
465 The pX459-sfCherry CRISPR-Cas9 vector were generated from pSpCas9(BB)-2A-Puro
466 (pX459) V2.0 (Addgene plasmid # 62988 ; http://n2t.net/addgene:62988 ;
467 RRID:Addgene_62988; a gift from Feng Zhang). The annealed oligonucleotides to
468 express single-guide RNA (sgRNA) against the *Rosa26* target sequence (70) was ligated
469 into pX459-sfCherry using the Ligation-Convenience Kit and designated as pX459-
470 sfCherry-sgRosa26-1.

471 We cloned a 1.6 kb genomic region upstream from start codon of mouse *Lmna*
472 as the endogenous promoter (-1407 to +249 bp from transcription start site) using
473 PrimeSTAR HS DNA Polymerase (Takara). Primers used in this study are listed in Table
474 S2. Mouse genomic DNA was extracted from cells by Proteinase K (Fungal; Invitrogen)
475 digestion according to the standard protocol and used for a PCR template. The CMV
476 promoter of mEmerald-C1 (Addgene plasmid # 53975 ; http://n2t.net/addgene:53975 ;
477 RRID:Addgene_53975; a gift from Michael Davidson) was replaced by the *Lmna*
478 promoter using the In-Fusion HD Cloning Kit (Clontech) and designated as pLmna-
479 mEmerald-C1. The mouse pre-LA cDNA was amplified from pPyCAG-LA-IP (71) using
480 the KOD One PCR Master Mix -Blue- (Toyobo), cloned into pLmna-mEmerald-C1 using
481 the In-Fusion, and designated as pLmna-Em-LA. The mouse PG cDNA was generated by
482 PrimeSTAR Max DNA Polymerase (Takara) to skip 150 bp, closed by In-Fusion HD, and
483 designated as pLmna-Em-PG. The amino acid truncation mutants were generated by PCR
484 mutagenesis using PrimeSTAR Max or PrimeSTAR HS DNA Polymerase. The LACS1
485 deletion mutant (Δ26) was generated using PrimeSTAR Max to skip 78 bp, and closed by
486 In-Fusion HD. The pLmna-Em-LA and pLmna-Em-PG expression cassettes were
487 amplified by the KOD One, fused with bGHpA amplified from LSL-Cas9-Rosa26TV

488 (Addgene plasmid # 61408 ; http://n2t.net/addgene:61408 ; RRID:Addgene_61408; a gift
489 from Feng Zhang) and *Pac* I/*Sma* I digested LSL-Cas9-Rosa26TV by In-Fusion HD, and
490 designated as pLmna-Em-LA-R26Neo, pLmna-Em-PG-R26Neo and pLmna-Em-PG-
491 CSM-R26Neo. The mouse LC cDNA was also generated by KOD One PCR and In-
492 Fusion HD and designated as pLmna-Em-LC-R26Neo.
493
494 **Cell culture**
495 MEFs isolated from WT and heterozygous c.1827C>T mutant (*Lmna*$^{G609G/+}$, G609G/+)
496 embryos at embryonic day 13.5 were generously gifted by Carlos López-Otín
497 (Universidad de Oviedo) (41, 42). Primary MEFs were cultured in modified DMEM (high
498 glucose; Nacalai Tesque) containing 10% FBS (qualified; Thermo Fisher), 4 mM L-
499 glutamine, 100 U/mL penicillin and 100 μg/mL streptomycin (Sigma-Aldrich), and 20
500 mM 2-[4-(2-Hydroxyethyl)-1-piperazinyl] ethanesulfonic acid (HEPES; Nacalai Tesque)
501 at 37°C in a humidified multi-gas incubator with 3% O_2/5% CO_2 (MCO-5M,
502 Sanyo/Panasonic Healthcare). Cells were immortalized by transduction with a retrovirus
503 expressing SV40 large T antigen from pBABE-puro largeTcDNA (Addgene plasmid #
504 14088 ; http://n2t.net/addgene:14088 ; RRID:Addgene_14088; a gift from William Hahn)
505 as previously described (13). After selection with 2 μg/ml puromycin (InvivoGen) for 4
506 d, immortalized WT and G609G/+ cells were cultured in growth medium without HEPES
507 at 37°C in a humidified chamber with 5% CO_2.
508
509 **Lentiviral transduction**
510 For lentivirus-mediated stable introduction of NLS^{SV40}-sfCherry-NLS^{Myc}, we followed
511 the methods that was previously described (30). Briefly, pVSV-G (PT3343-5, Clontech)
512 and psPAX2 (Addgene plasmid #12260; http://n2t.net/addgene:12260;
513 RRID:Addgene_12260; a gift from Didier Trono), together with a pCDH vector (pCDH-
514 NLS^{SV40}-sfCherry-NLS^{Myc}-Blast, pCDH-NLS^{SV40}-sfCherry-NLS^{Myc}-Hygro or pCDH-
515 sfGFP-DARPin-LA6-Hygro) in a 1:3:4 weight ratio of each plasmid was transfected into
516 ~80% confluent 293T cells (CRL-3216, ATCC) using Lipofectamine 3000 following the
517 manufacturer's instructions for lentivirus production. 24 h after the transfection, the
518 medium was replaced with fresh medium, and the virus-containing culture supernatant
519 was harvested at 48 h after transfection and filtrated with a 0.45-μm syringe filter. For

520 virus infection, MEFs were incubated in the culture supernatants with 4 μg/mL polybrene
521 (Nacalai Tesque) for 24 h. Infected cells were selected by incubation in medium
522 containing 3 μg/mL blasticidin S or 200 μg/mL hygromycin B Gold (InvivoGen) for 4 d.
523

524 **Live-cell imaging and NE rupture induction by laser microirradiation**

525 Culture medium was replaced with FluoroBrite DMEM (Thermo Fisher) containing 10%
526 FBS, 4 mM L-glutamine, 100U/mL penicillin and 100 μg/mL streptomycin. For laser-
527 microirradiation and image acquisition, cells were set onto a heated stage (37°C; Tokai
528 Hit) with a CO_2-control system (Tokken) on a confocal microscope (FV1000, Olympus)
529 with a 60× PlanApo N (NA 1.4) oil lens operated by built-in software FLUOVIEW ver.
530 4.2 (Olympus). All live-cell images were acquired using a main scanner (4% 488-nm laser
531 transmission; 30% 543-nm laser transmission; 2 μs/pixel; 512×512 pixels; pinhole 100
532 μm; 6× zoom; ~10 s/frame). After the first image was acquired, a 2 μm diameter spot was
533 laser-microirradiated using a second scanner at 100% power of 405-nm laser transmission
534 (40 μs/pixel; approximately 780 μW) for 10 s whereas the images were acquired with
535 another scanner.

536 Fiji software (ImageJ) ver. 1.53v (National Institute of Health) was used for
537 measuring max intensity at the sites of NE rupture after Gaussian filtering with $\sigma = 2.0$
538 over time. Fluorescence intensity was normalized by each of the initial intensity in the
539 laser-microirradiated region.

540 CellProfiler ver. 3.1.9 (Broad Institute) with the NP_NL_intensity_live pipeline
541 (uploaded on GitHub; http://github.com/Kimura-Lab/Kono-et-al.-2023) (30) were used
542 for measuring mean intensity of mEmerald-LA mutants and mEmerald-LC in the NP and
543 the NL. Briefly, after the nuclear region was recognized by the nuclear localization of
544 NLS-sfCherry, 3 pixels (207 nm) and more than 10 pixels (690 nm) inside from the rim
545 of nuclear region were regarded as the NL and the NP, respectively, and then the mean
546 intensity of each section was measured. All images were processed in Photoshop ver. 24
547 (Adobe) for cropping and brightness/contrast adjustment.
548

549 **Indirect immunofluorescence and microscopy**

550 Primary antibodies used for immunofluorescence were mouse monoclonal anti-LA
551 (1:250; 4A58, sc-71481, Santa Cruz), rat monoclonal anti-pre-LA (1:1,000; 7G11;
552 MABT345, EMD Millipore; (49)), mouse monoclonal anti-mature-LA (1:8,000; 4A4-A4,
553 14-9848-82, Invitrogen; (72)), rabbit polyclonal anti-progerin (1:1000; generated by the
554 Nourshargh laboratory using a peptide immunogen of murine progerin and standard
555 immunization procedures; (63, 73, 74)), mouse monoclonal anti-LB1 (1:1,000; B-10; sc-
556 374015, Santa Cruz), rabbit monoclonal anti-cGAS (1:250; D3O8O; 21659, Cell
557 Signaling Technology) and rabbit monoclonal anti-BANF1/BAF (1:200; EPR7668;
558 ab129184, Abcam). The secondary antibodies used were Alexa Fluor 488-donkey anti-
559 mouse immunoglobulin G (IgG), Alexa Fluor 488-donkey anti-rabbit IgG (1:2,000;
560 A21202 and 1:2,000; A21206, respectively, Thermo Fisher), Cy5-donkey anti-mouse IgG
561 and Cy5-goat anti-rat IgG (1:2,000; 715-175-151 and 1:2,000; 712-175-153, respectively,
562 Jackson ImmunoResearch).

563 Cells were grown on 35-mm Glass Based Dishes which have a cover glass with
564 a grid pattern (IWAKI) and fixed after laser-microirradiation with 4% PFA (Electron
565 Microscopy Sciences) containing 0.1% Triton X-100 (Nacalai Tesque) for 15 min,
566 followed by permeabilization using 0.1% Triton X-100 in PBS for 10 min and then
567 blocking with Blocking One-P (Nacalai Tesque) for 30 min. Cells were incubated with
568 primary antibodies overnight at 4°C, washed with 10% Blocking One-P in PBS, and
569 incubated with secondary antibodies for 1 h at RT. DNA was stained with Hoechst 33342
570 (0.5 μg/mL; Thermo Fisher). For Fig. S1 A, cells were fixed with 4% PFA for 15 min,
571 followed by permeabilization using 0.1% Triton X-100 in PBS for 10 min and then
572 blocking with Blocking One-P for 30 min. After incubation with primary antibodies, the
573 RFP-Booster Alexa Fluor 568 (alpaca monoclonal anti-RFP Nanobody; 1:1000;
574 rb2AF568, ChromoTek) was used with second antibodies to amplify the signal of NLS-
575 sfCherry.

576 Confocal fluorescence images were obtained using a confocal microscope
577 FV1000 with a 60× PlanApo N (NA 1.4) oil lens (3.0% 405-nm laser transmission; 3.1-
578 11.1% 488-nm laser transmission; 5.0% 543-nm laser transmission; 1.0-4.0% 633-nm
579 laser transmission; 2 μs/pixel; 512×512 pixels; pinhole 100 μm). CellProfiler with the
580 NP_NL_intensity_fixed pipeline (uploaded on GitHub; http://github.com/Kimura-

581 Lab/Kono-et-al.-2023) were used for measuring mean intensity of lamins in the NP and
582 the NL. The nuclear region was recognized by staining DNA with Hoechst 33342.
583
584 **Induction of mechanical NE rupture by atomic force microscopy (AFM)**
585 Culture medium was replaced with Leibovitz's L-15 medium (no phenol red; Thermo
586 Fisher) containing 10% FBS, 2 mM L-glutamine, 100U/mL penicillin and 100 μg/mL
587 streptomycin. JPK NanoWizard 4 BioAFM (Bruker) incorporated into an inverted
588 fluorescence microscope (Eclipse Ti2, Nikon) with EM-CCD camera (iXon Ultra 888,
589 Andor) and light source (X-Cite XYLIS, Excelitas) was used for single-cell compression.
590 Cantilever (TL-CONT, Nanosensors; spring constant approximately 0.2 N/m) with a 100-
591 μm glass bead (BZ-01, As-One) was used for NE rupture. Cells expressing NLS-sfCherry
592 were set onto a heated stage (37°C) and the first fluorescent image of NLS-sfCherry was
593 obtained before the rupture using a TRITC filter and NIS-Elements BR (Nikon). Next,
594 the bead was approached on the top of the cell surface with 2 nN setpoint and then forced
595 down for 5 μm. After waiting for 10 s, the cantilever was retracted. Within 10 s after the
596 retraction, time-lapse imaging was started with 30 s exposure time every 30 s for 5 min.
597 Fiji software (ImageJ) was used for measuring mean intensities in the region of interest
598 from nucleoplasm and cytoplasm.
599
600 **Chemicals**
601 As a selective farnesyltransferase inhibitor (FTI), lonafarnib (SCH66336; Merck) was
602 dissolved in dimethylsulfoxide (DMSO; Nacalai Tesque) and added to the cells with one
603 daily dose of 3.2 μM for 2 days. For controls in all experiments, an equal volume of
604 vehicle (0.1% DMSO) was added.
605
606 **Immunoblotting**
607 For immunoblotting, we followed the methods that were previously described (30).
608 Briefly, primary antibodies used for immunoblotting were mouse monoclonal anti-LA/C
609 (1:5,000-20,000; 3A6-4C11, 14-9847-82, eBioscience), rat monoclonal anti-pre-LA
610 (1:1,000; 7G11), rabbit polyclonal anti-progerin (1:1,000; Nourshargh lab), rabbit
611 monoclonal anti-BANF1/BAF (1:500; EPR7668, Abcam), anti-β-Actin (1:2,000; AC-15,

612 sc-69879, Santa Cruz) and anti-GAPDH (1:5,000; 6C5, sc-32233, Santa Cruz). The
613 secondary antibodies used were anti-mouse IgG HRP-linked whole Ab sheep (1:10,000;
614 NA931, Amersham), anti-rabbit IgG HRP-linked $F(ab')_2$ fragment donkey (1:10,000;
615 NA9340, Amersham) and HRP-donkey anti-rat IgG (H+L) (1:10,000; 712-035-150,
616 Jackson ImmunoResearch).
617
618 **Rosa26-targeted gene knock-in**
619 The pLmna-Em-preLA-R26Neo, pLmna-Em-PG-R26Neo and pLmna-Em-LC-R26Neo
620 were linearized by the *Kpn* I (Takara) and purified by phenol/chloroform extraction and
621 ethanol precipitation. Cells were transfected with appropriate plasmids using
622 Lipofectamine 3000 (Thermo Fisher) by reverse transfection as previously described (30).
623 Briefly, the DNA-lipid complex (3 μg linearized *Rosa26* targeting vectors : 2 μg pX459-
624 sfCherry-sgRosa26-1 : 7.5 μL Lipofectamine 3000 in 250 μL Opti-MEM; Thermo Fisher)
625 was added to 1.62×10^5 cells as they were seeding onto a 35 mm dish with 2 mL of growth
626 medium. One day after the transfection, the medium was replaced with fresh medium.
627 Two days after the transfection, cells were selected by incubation in medium containing
628 400 μg/mL G-418 disulfate aqueous solution (Nacalai Tesque) for 7 d.
629
630 **Fluorescence Correlation Spectroscopy (FCS)**
631 FCS measurements were all performed at 25°C with an LSM780 confocal microscope
632 (Carl Zeiss) as previously described (15, 46, 75). FCS setups using the LSM780
633 microscope consisted of a continuous-wave Ar^+ laser (25 mW), a water-immersion
634 objective (C-Apochromat, ×40/1.2 NA; Carl Zeiss), and a GaAsP multichannel spectral
635 detector (Quasar; Carl Zeiss). Fluorescent protein of mEmerald was excited with the 488-
636 nm laser line with a minimal laser power (0.5%) to allow an optimal signal-to-noise ratio.
637 Diameter of pinhole was adjusted to 34 μm (1 Airy unit) for the 488-nm laser. Emission
638 fluorescence was detected at 500–550 nm in the green channel. The structure parameter
639 and detection volume were calibrated using Rhodamine-6G (Sigma-Aldrich) solution
640 with diffusion coefficient (280 $\mu m^2/s$; 25°C in water) before experiments with cells. For
641 FCS measurement, three positions were randomly selected inside the nucleoplasm, and
642 molecular diffusion was measured for 10 s five times. The first round of the five
643 repetitions were carried out to photobleach immobile fraction, and then the four

644 repetitions were used for further analysis. FCS data were analyzed with analytical
645 software installed in the ZEN 2012 SP5 FP1 (black) acquisition software (Carl Zeiss) (46,
646 75). Briefly, all measured fluorescence auto-correlation functions (FAFs) from live cells
647 were globally fitted by the ConfoCor3 software installed on LSM780 system using fitting
648 models considering three-dimensional free diffusion with a Gaussian laser profile,
649 including a triplet component to estimate the diffusion coefficient.
650
651 **Generation of the Zmpste24- and BAF-KD MEFs**
652 MEFs expressing shRNAs of anti-Zmpste24 and anti-BAF were generated through
653 lentiviral transduction. KD by shRNA expression was carried out by Lentivirus
654 transduction (see the section on Lentiviral transduction above) and 3 d selection with 3
655 μg/mL blasticidin S Gold for pLKO.3-blast.
656
657 **Statistical analyses**
658 Unless mentioned otherwise, all plots showed mean values ± SEM (error bars). Fisher's
659 exact test was performed to analyze the categorical data using EZR on R commander ver.
660 1.61 (programmed by Yoshinobu Kanda) (76). The mixed effect model fit by restricted
661 maximum likelihood (REML) was performed to analyze the interaction between group
662 and time using the *lme4* (77) and the *lmerTest* (78) packages in EZR, where cell's id was
663 set as a random effect, while group and time as fixed effects. The interaction between
664 group and time (group × time) was also set as a fixed effect. The Welch's t-test or the
665 Welch's one-way ANOVA followed by the Games–Howell post-hoc test was performed
666 to single or multiple comparison, respectively. Statistic codes for R ver. 4.2.2 and a
667 modified R commander for EZR 1.61 are uploaded on GitHub
668 (http://github.com/Kimura-Lab/Kono-et-al.-2023). Significance was determined if $P <$
669 0.05.

670 **Supplemental material**

671 Table S1 shows the phenotype characterization in WT and G609G/+ cells by
672 immunofluorescence. Table S2 shows oligonucleotide sequences used in this study. Fig.
673 S1 shows the immunofluorescence of WT and G609G/+ cells for phenotype
674 characterization, and the localization of LA and PG to the rupture sites within 10 min, and
675 at 30-40 and 120-130 min after laser microirradiation. Fig. S2 shows the protein
676 architecture of A-type lamins and DARPin-LA6, and localization kinetics of DARPin-
677 LA6 at the rupture sites in WT and G609G/+ cells. Fig. S3 shows WT and G609G/+ cells
678 expressing A-type lamins under the *Lmna* promoter knocked-in to *Rosa26* locus and FCS
679 analysis for mEmerald-LC. Fig. S4 shows the localization of LA and PG to the rupture
680 sites within 10 min in FTI-treated WT and G609G/+ nuclei. Fig. S5 shows the
681 immunoblotting of FTI-treated WT and G609G/+ cells expressing A-type lamins under
682 the *Lmna* promoter knocked-in to *Rosa26* locus, and the representative image of FCS
683 analysis. Fig. S6 shows immunoblotting, immunofluorescence and the localization of LA
684 and pre-LA to the rupture sites in Zmpste24-KD cells. Fig. S7 shows the differences
685 between LA and LC amino acid sequence, and dynamics of LA mutants at the rupture
686 sites, and the NP/NL ratios of mEmerald-LA mutants by live-cell imaging.

Acknowledgments

We would like to thank Prof. Carlos López-Otín (Universidad de Oviedo) for providing us with the primary MEFs isolated from WT and *Lmna* c.1827C>T mutant (*Lmna*$^{G609G/+}$ and *Lmna*$^{G609G/G609G}$) embryos. We thank Biomaterials Analysis Division, Open Facility Center (OFC) of Tokyo Institute of Technology for nucleotide sequencing and sharing research equipment, especially Carl Zeiss ElyraS1/Airyscan/LSM780 is shared in MEXT Project Grant Number JPMXS0440200022. We also thank the Cellular Imaging Core Facility at the ConveRgence mEDIcine research cenTer (CREDIT), Asan Medical Center for technical support. The generation and validation of the anti-murine progerin antibody was funded by the Wellcome Trust (098291/Z/12/Z to S. Nourshargh) and the British Heart Foundation (FS/IBSRF/22/25121 to L. Rolas). We also acknowledge the R statistic code generated by Shinsuke Hatano (Ryukoku University). We also thank all members of the Kimura lab at Tokyo Institute of Technology and Tokuko Haraguchi (Osaka University) for advice and discussions. This work was supported by JSPS KAKENHI Grant Numbers JP20KK0158 (to T. Shimi, Y. Kono, K. Miyazawa and H. Kimura), JP20K06617 (to T. Shimi), and JP18H05527 and JP21H04764 (to H. Kimura). This work was also supported by MEXT (World Premier International Research Center Initiative [WPI]). Y. Kono was an academy scholar at the Specialized Academy for Cell Science (Ohsumi-juku) of the Tokyo Tech Organization for Fundamental Research (OFR). The authors declare no competing financial interests.

Author contributions

T. Shimi conceived the project. Y. Kono designed, performed and interpreted experiments. C.G. Pack performed FCS experiments. T. Ichikawa performed AFM experiments. A. Komatsubara performed image analysis. L. Rolas and S. Nourshargh generated, characterized, and provided the anti-murine progerin antibody. S.A. Adam, K. Miyazawa, O. Medalia and R.D. Goldman provided advice and scientific discussion. Y. Kono, C.G. Pack, T. Ichikawa and T. Shimi drafted the manuscript. S.A. Adam, R.D. Goldman, and H. Kimura edited the manuscript. T. Shimi, S.A. Adam, T. Fukuma, H. Kimura and R.D. Goldman supervised the experiments.

717 ## References

718 1. J. M. Zullo *et al.*, DNA sequence-dependent compartmentalization and silencing of chromatin at
719 the nuclear lamina. *Cell* **149**, 1474-1487 (2012).
720 2. M. Crisp *et al.*, Coupling of the nucleus and cytoplasm: role of the LINC complex. *J Cell Biol* **172**,
721 41-53 (2006).
722 3. G. K. Voeltz, M. M. Rolls, T. A. Rapoport, Structural organization of the endoplasmic reticulum.
723 *EMBO Rep* **3**, 944-950 (2002).
724 4. P. L. Paine, L. C. Moore, S. B. Horowitz, Nuclear envelope permeability. *Nature* **254**, 109-114
725 (1975).
726 5. R. Foisner, L. Gerace, Integral Membrane-Proteins of the Nuclear-Envelope Interact with Lamins
727 and Chromosomes, and Binding Is Modulated by Mitotic Phosphorylation. *Cell* **73**, 1267-1279
728 (1993).
729 6. L. Gerace, A. Blum, G. Blobel, Immunocytochemical localization of the major polypeptides of the
730 nuclear pore complex-lamina fraction. Interphase and mitotic distribution. *J Cell Biol* **79**, 546-566
731 (1978).
732 7. L. Gerace, G. Blobel, The nuclear envelope lamina is reversibly depolymerized during mitosis.
733 *Cell* **19**, 277-287 (1980).
734 8. F. Lin, H. J. Worman, Structural organization of the human gene encoding nuclear lamin A and
735 nuclear lamin C. *J Biol Chem* **268**, 16321-16326 (1993).
736 9. T. H. Höger, K. Zatloukal, I. Waizenegger, G. Krohne, Characterization of a second highly
737 conserved B-type lamin present in cells previously thought to contain only a single B-type lamin.
738 *Chromosoma* **99**, 379-390 (1990).
739 10. G. Biamonti *et al.*, The gene for a novel human lamin maps at a highly transcribed locus of
740 chromosome 19 which replicates at the onset of S-phase. *Mol Cell Biol* **12**, 3499-3506 (1992).
741 11. F. Lin, H. J. Worman, Structural organization of the human gene (LMNB1) encoding nuclear lamin
742 B1. *Genomics* **27**, 230-236 (1995).
743 12. H. Maeno, K. Sugimoto, N. Nakajima, Genomic structure of the mouse gene (Lmnb1) encoding
744 nuclear lamin B1. *Genomics* **30**, 342-346 (1995).
745 13. T. Shimi *et al.*, Structural organization of nuclear lamins A, C, B1, and B2 revealed by
746 superresolution microscopy. *Mol Biol Cell* **26**, 4075-4086 (2015).
747 14. Y. Turgay *et al.*, The molecular architecture of lamins in somatic cells. *Nature* **543**, 261-264 (2017).
748 15. T. Shimi *et al.*, The A- and B-type nuclear lamin networks: microdomains involved in chromatin
749 organization and transcription. *Genes Dev* **22**, 3409-3421 (2008).
750 16. M. Kittisopikul *et al.*, Computational analyses reveal spatial relationships between nuclear pore
751 complexes and specific lamins. *J Cell Biol* **220** (2021).

752 17. R. J. Lutz, M. A. Trujillo, K. S. Denham, L. Wenger, M. Sinensky, Nucleoplasmic localization of
753 prelamin A: implications for prenylation-dependent lamin A assembly into the nuclear lamina.
754 *Proc Natl Acad Sci U S A* **89**, 3000-3004 (1992).
755 18. M. Sinensky *et al.*, The processing pathway of prelamin A. *J Cell Sci* **107 (Pt 1)**, 61-67 (1994).
756 19. V. L. Boyartchuk, M. N. Ashby, J. Rine, Modulation of Ras and a-factor function by carboxyl-
757 terminal proteolysis. *Science* **275**, 1796-1800 (1997).
758 20. A. M. Winter-Vann, P. J. Casey, Post-prenylation-processing enzymes as new targets in
759 oncogenesis. *Nat Rev Cancer* **5**, 405-412 (2005).
760 21. G. K. Leung *et al.*, Biochemical studies of Zmpste24-deficient mice. *J Biol Chem* **276**, 29051-
761 29058 (2001).
762 22. D. P. Corrigan *et al.*, Prelamin A endoproteolytic processing in vitro by recombinant Zmpste24.
763 *Biochem J* **387**, 129-138 (2005).
764 23. C. M. Denais *et al.*, Nuclear envelope rupture and repair during cancer cell migration. *Science* **352**,
765 353-358 (2016).
766 24. M. Raab *et al.*, ESCRT III repairs nuclear envelope ruptures during cell migration to limit DNA
767 damage and cell death. *Science* **352**, 359-362 (2016).
768 25. C. T. Halfmann *et al.*, Repair of nuclear ruptures requires barrier-to-autointegration factor. *J Cell*
769 *Biol* **218**, 2136-2149 (2019).
770 26. J. D. Vargas, E. M. Hatch, D. J. Anderson, M. W. Hetzer, Transient nuclear envelope rupturing
771 during interphase in human cancer cells. *Nucleus* **3**, 88-100 (2012).
772 27. J. Robijns *et al.*, In silico synchronization reveals regulators of nuclear ruptures in lamin A/C
773 deficient model cells. *Sci Rep* **6**, 30325 (2016).
774 28. N. Y. Chen *et al.*, Fibroblasts lacking nuclear lamins do not have nuclear blebs or protrusions but
775 nevertheless have frequent nuclear membrane ruptures. *Proc Natl Acad Sci U S A* **115**, 10100-
776 10105 (2018).
777 29. N. Y. Chen *et al.*, An absence of lamin B1 in migrating neurons causes nuclear membrane ruptures
778 and cell death. *Proc Natl Acad Sci U S A* **116**, 25870-25879 (2019).
779 30. Y. Kono *et al.*, Nucleoplasmic lamin C rapidly accumulates at sites of nuclear envelope rupture
780 with BAF and cGAS. *J Cell Biol* **221** (2022).
781 31. H. J. Worman, G. Bonne, "Laminopathies": a wide spectrum of human diseases. *Exp Cell Res* **313**,
782 2121-2133 (2007).
783 32. W. H. De Vos *et al.*, Repetitive disruptions of the nuclear envelope invoke temporary loss of
784 cellular compartmentalization in laminopathies. *Hum Mol Genet* **20**, 4175-4186 (2011).
785 33. A. J. Earle *et al.*, Mutant lamins cause nuclear envelope rupture and DNA damage in skeletal
786 muscle cells. *Nat Mater* **19**, 464-473 (2020).
787 34. P. H. Kim *et al.*, Nuclear membrane ruptures underlie the vascular pathology in a mouse model of

Hutchinson-Gilford progeria syndrome. *JCI Insight* **6** (2021).

35. A. De Sandre-Giovannoli *et al.*, Lamin a truncation in Hutchinson-Gilford progeria. *Science* **300**, 2055 (2003).

36. M. Eriksson *et al.*, Recurrent de novo point mutations in lamin A cause Hutchinson-Gilford progeria syndrome. *Nature* **423**, 293-298 (2003).

37. A. M. Young, A. L. Gunn, E. M. Hatch, BAF facilitates interphase nuclear membrane repair through recruitment of nuclear transmembrane proteins. *Mol Biol Cell* **31**, 1551-1560 (2020).

38. R. M. Sears, K. J. Roux, Mechanisms of A-Type Lamin Targeting to Nuclear Ruptures Are Disrupted in LMNA- and BANF1-Associated Progerias. *Cells* **11** (2022).

39. O. A. Zhironkina *et al.*, Mechanisms of nuclear lamina growth in interphase. *Histochem Cell Biol* **145**, 419-432 (2016).

40. S. Cho *et al.*, Progerin phosphorylation in interphase is lower and less mechanosensitive than lamin-A,C in iPS-derived mesenchymal stem cells. *Nucleus* **9**, 230-245 (2018).

41. I. C. Lopez-Mejia *et al.*, A conserved splicing mechanism of the LMNA gene controls premature aging. *Hum Mol Genet* **20**, 4540-4555 (2011).

42. F. G. Osorio *et al.*, Splicing-directed therapy in a new mouse model of human accelerated aging. *Sci Transl Med* **3**, 106ra107 (2011).

43. I. L. Ivanovska, M. P. Tobin, T. Bai, L. J. Dooling, D. E. Discher, Small lipid droplets are rigid enough to indent a nucleus, dilute the lamina, and cause rupture. *J Cell Biol* **222** (2023).

44. M. Zwerger *et al.*, Altering lamina assembly reveals lamina-dependent and -independent functions for A-type lamins. *J Cell Sci* **128**, 3607-3620 (2015).

45. V. Kochin *et al.*, Interphase phosphorylation of lamin A. *J Cell Sci* **127**, 2683-2696 (2014).

46. T. Shimi, C. G. Pack, R. D. Goldman, Analyses of the Dynamic Properties of Nuclear Lamins by Fluorescence Recovery After Photobleaching (FRAP) and Fluorescence Correlation Spectroscopy (FCS). *Methods Mol Biol* **1411**, 99-111 (2016).

47. D. Holtz, R. A. Tanaka, J. Hartwig, F. McKeon, The CaaX motif of lamin A functions in conjunction with the nuclear localization signal to target assembly to the nuclear envelope. *Cell* **59**, 969-977 (1989).

48. M. H. Gelb *et al.*, Therapeutic intervention based on protein prenylation and associated modifications. *Nat Chem Biol* **2**, 518-528 (2006).

49. R. Lee *et al.*, Genetic studies on the functional relevance of the protein prenyltransferases in skin keratinocytes. *Hum Mol Genet* **19**, 1603-1617 (2010).

50. S. Y. Chang *et al.*, Inhibitors of protein geranylgeranyltransferase-I lead to prelamin A accumulation in cells by inhibiting ZMPSTE24. *J Lipid Res* **53**, 1176-1182 (2012).

51. H. Yao *et al.*, Targeting RAS-converting enzyme 1 overcomes senescence and improves progeria-like phenotypes of ZMPSTE24 deficiency. *Aging Cell* **19**, e13200 (2020).

824 52. X. Chen *et al.*, A small-molecule ICMT inhibitor delays senescence of Hutchinson-Gilford
825 progeria syndrome cells. *Elife* **10** (2021).
826 53. K. N. Dahl *et al.*, Distinct structural and mechanical properties of the nuclear lamina in
827 Hutchinson-Gilford progeria syndrome. *Proc Natl Acad Sci U S A* **103**, 10271-10276 (2006).
828 54. A. Quigley *et al.*, The structural basis of ZMPSTE24-dependent laminopathies. *Science* **339**, 1604-
829 1607 (2013).
830 55. K. R. Yu *et al.*, MicroRNA-141-3p plays a role in human mesenchymal stem cell aging by directly
831 targeting ZMPSTE24. *J Cell Sci* **126**, 5422-5431 (2013).
832 56. L. G. Fong *et al.*, Heterozygosity for Lmna deficiency eliminates the progeria-like phenotypes in
833 Zmpste24-deficient mice. *Proc Natl Acad Sci U S A* **101**, 18111-18116 (2004).
834 57. A. Casasola *et al.*, Prelamin A processing, accumulation and distribution in normal cells and
835 laminopathy disorders. *Nucleus* **7**, 84-102 (2016).
836 58. R. D. Goldman *et al.*, Accumulation of mutant lamin A causes progressive changes in nuclear
837 architecture in Hutchinson-Gilford progeria syndrome. *Proc Natl Acad Sci U S A* **101**, 8963-8968
838 (2004).
839 59. T. Shimi *et al.*, The role of nuclear lamin B1 in cell proliferation and senescence. *Genes Dev* **25**,
840 2579-2593 (2011).
841 60. A. Ivanov *et al.*, Lysosome-mediated processing of chromatin in senescence. *J Cell Biol* **202**, 129-
842 143 (2013).
843 61. Z. Dou *et al.*, Autophagy mediates degradation of nuclear lamina. *Nature* **527**, 105-109 (2015).
844 62. P. Scaffidi, T. Misteli, Reversal of the cellular phenotype in the premature aging disease
845 Hutchinson-Gilford progeria syndrome. *Nat Med* **11**, 440-445 (2005).
846 63. O. Santiago-Fernández *et al.*, Development of a CRISPR/Cas9-based therapy for Hutchinson-
847 Gilford progeria syndrome. *Nat Med* **25**, 423-426 (2019).
848 64. J. L. V. Broers *et al.*, Dynamics of the nuclear lamina as monitored by GFP-tagged A-type lamins.
849 *J Cell Sci* **112 (Pt 20)**, 3463-3475 (1999).
850 65. T. Haraguchi *et al.*, Nuclear localization of barrier-to-autointegration factor is correlated with
851 progression of S phase in human cells. *J Cell Sci* **120**, 1967-1977 (2007).
852 66. T. Haraguchi *et al.*, Live cell imaging and electron microscopy reveal dynamic processes of BAF-
853 directed nuclear envelope assembly. *J Cell Sci* **121**, 2540-2554 (2008).
854 67. V. Stierlé *et al.*, The carboxyl-terminal region common to lamins A and C contains a DNA binding
855 domain. *Biochemistry* **42**, 4819-4828 (2003).
856 68. A. C. Schibler, P. Jevtic, G. Pegoraro, D. L. Levy, T. Misteli, Identification of epigenetic
857 modulators as determinants of nuclear size and shape. *Elife* **12**, 10.1101/2022.1105.1128.493845
858 (2023).
859 69. K. Ikegami, S. Secchia, O. Almakki, J. D. Lieb, I. P. Moskowitz, Phosphorylated Lamin A/C in

860 the Nuclear Interior Binds Active Enhancers Associated with Abnormal Transcription in Progeria.
861 *Dev Cell* **52**, 699-713 e611 (2020).
862 70. V. T. Chu *et al.*, Increasing the efficiency of homology-directed repair for CRISPR-Cas9-induced
863 precise gene editing in mammalian cells. *Nat Biotechnol* **33**, 543-548 (2015).
864 71. Y. Guo, Y. Kim, T. Shimi, R. D. Goldman, Y. Zheng, Concentration-dependent lamin assembly
865 and its roles in the localization of other nuclear proteins. *Mol Biol Cell* **25**, 1287-1297 (2014).
866 72. M. Roblek *et al.*, Monoclonal antibodies specific for disease-associated point-mutants: lamin A/C
867 R453W and R482W. *PLoS One* **5**, e10604 (2010).
868 73. B. Marcos-Ramiro *et al.*, Isoprenylcysteine Carboxylmethyltransferase-Based Therapy for
869 Hutchinson-Gilford Progeria Syndrome. *ACS Cent Sci* **7**, 1300-1310 (2021).
870 74. A. Sánchez-López *et al.*, Cardiovascular Progerin Suppression and Lamin A Restoration Rescue
871 Hutchinson-Gilford Progeria Syndrome. *Circulation* **144**, 1777-1794 (2021).
872 75. H. Park, S. S. Han, Y. Sako, C. G. Pack, Dynamic and unique nucleolar microenvironment revealed
873 by fluorescence correlation spectroscopy. *FASEB J* **29**, 837-848 (2015).
874 76. Y. Kanda, Investigation of the freely available easy-to-use software 'EZR' for medical statistics.
875 *Bone Marrow Transplant* **48**, 452-458 (2013).
876 77. D. Bates, M. Mächler, B. M. Bolker, S. C. Walker, Fitting Linear Mixed-Effects Models Using
877 lme4. *Journal of Statistical Software* **67**, 1-48 (2015).
878 78. A. Kuznetsova, P. B. Brockhoff, R. H. B. Christensen, lmerTest Package: Tests in Linear Mixed
879 Effects Models. *Journal of Statistical Software* **82**, 1-26 (2017).
880 79. M. Mirdita *et al.*, ColabFold: making protein folding accessible to all. *Nat Methods* **19**, 679-682
881 (2022).

882 **Abbreviations**

883 BAF, barrier-to-autointegration factor; CBD, chromatin-binding domain; cGAS, cyclic
884 GMP-AMP synthase; DARPin, designed ankyrin repeat protein; DCM, dilated
885 cardiomyopathy; ESCRT-III, endosomal sorting complex required for transport-III; ER,
886 endoplasmic reticulum; FAF, fluorescence auto-correlation function; FCS, fluorescence
887 correlation spectroscopy; FTI, farnesyltransferase inhibitor; FPLD, familial partial
888 lipodystrophy; HGPS, Hutchinson-Gilford Progeria syndrome; Ig-fold, immunoglobulin-
889 like fold; INM, inner nuclear membrane; KD, knockdown; KO, knockout; LA, lamin A;
890 LACS, LA-characteristic sequence; LB1, lamin B1; LB2, lamin B2; LC, lamin C; LINC,
891 linker of nucleoskeleton and cytoskeleton; MEF, mouse embryonic fibroblast; MD,
892 muscular dystrophy; NE, nuclear envelope; NL, nuclear lamina; NP, nucleoplasmic pool;
893 NPC, nuclear pore complex; ONM, outer nuclear membrane; PG, progerin; REML,
894 restricted maximum likelihood; sfGFP, superfolder GFP; sfCherry, superfolder Cherry;
895 shRNA, short hairpin RNA; STING, stimulator of interferon genes; WT, wild type.

896 ## Figure legends

897 Figure 1. **The localization kinetics of LA and PG at the rupture sites in WT and**
898 **G609G/+ nuclei. (A)** Protein architecture of LA and PG. The coiled-coil central rod
899 domain (gray), the NLS (yellow), the β-strand comprising the Ig-fold domain (blue), and
900 the CaaX motif (orange) are shown in the diagram. Anti-LA (4A58) and anti-PG do not
901 cross-react with each other. Anti-pre-LA (7G11) recognizes the last amino acids that is
902 proteolytically cleaved off and does not react with PG. Anti-mature-LA (4A4-A4)
903 recognizes mature-LA but not pre-LA. Anti-LA/C (3A6-4C11) recognizes all A-type
904 lamin isoforms. **(B)** NE rupture was induced by AFM indentation using a cantilever with
905 a round tip, as shown in the diagram. **(C** and **D)** Time-lapse images of NLS-sfCherry
906 expressed in WT and G609G/+ cells were acquired with 30 s intervals for 5 min after the
907 induction of NE rupture by AFM indentation. **(C)** The fluorescence intensities in the cells
908 are shown with rainbow color. Bar: 10 μm. **(D)** The nuclear-to-cytoplasmic intensity
909 (N/C) ratios of NLS-sfCherry were measured and normalized to the initial intensities, and
910 plotted to monitor the nuclear reentry in the cells (means ± SEM; n = 20 cells from two
911 independent experiments; ***, $P < 0.001$ from WT by a mixed effect model). **(E)** NE
912 rupture was induced by 405-nm laser microirradiation with a 2-μm diameter spot at the
913 NE of WT and G609G/+ nuclei. **(F** and **G)** 13 to 21 of nuclei of the cells were laser-
914 microirradiated within 10 min and incubated for 0, 30, 60 and 120 min, followed by
915 fixation with 4% PFA/0.1% Triton-X 100. The fixed cells were immunostained with a
916 combination of the LA and PG antibodies, and the DNA was stained with Hoechst 33342.
917 **(F)** Representative confocal images of nuclei in the cells fixed within 60-70 min after the
918 induction of NE rupture by laser microirradiation. Magnified views of the areas indicated
919 with orange boxes are shown (bottom). The rupture sites are indicated with yellow
920 arrowheads (bottom). Bars: 5 μm (top) and 2μm (bottom). **(G)** Percentiles of the cells
921 with (blue) and without (gray) the localization of LA and PG to the rupture sites. The
922 numbers of analyzed cells from two independent experiments are indicated in the bar
923 charts. The line graphs show the kinetics of the percentage of the cells with localization
924 of LA and PG to the rupture sites.
925
926 Figure 2. **Localization of LA and PG to the rupture sites in DMSO or FTI-treated**
927 **WT and G609G/+ nuclei. (A)** Whole cell lysates from WT and G609G/+ cells treated
928 with 0.1% DMSO or 3.2 μM lonafarnib (FTI) were probed with anti-LA/C (3A6-4C11),
929 anti-PG, and anti-GAPDH (as loading control) for immunobloting. Positions of the size
930 standards are shown on the right. **(B** and **C)** The indicated cells were immunostained with
931 the LA (4A58) and PG antibodies. **(B)** Representative microscopic images. **(C)** Ratios of
932 the average fluorescence intensity in the nucleoplasmic pool relative to that of the NL
933 (NP/NL ratios) of LA and PG were measured based on immunofluorescence (n = 20 cells

934 from two independent experiments; ***, P < 0.001 by Welch's t-tests). **(D)** 15 to 19 of
935 nuclei in the cells were laser-microirradiated and incubated for 60 min, followed by
936 fixation with 4% PFA/0.1% Triton-X 100. The fixed cells were immunostained with a
937 combination of the LA and PG antibodies. Percentiles of the cells with (blue) and without
938 (gray) the localization of LA and PG at the rupture sites. The numbers of analyzed cells
939 from two independent experiments are indicated in the bar charts.
940
941 Figure 3. **The diffusion kinetics of LA and PG in the nucleoplasm of DMSO or FTI-**
942 **treated WT and G609G/+ nuclei.** The diffusion fractions of mEmerald-LA (Em-LA)
943 and mEmerald-PG (Em-PG) in DMSO- or FTI-treated WT and G609G/+ nuclei were
944 measured by FCS. **(A)** A representative confocal image of a WT nucleus with Em-LA
945 before FCS measurements (left). The yellow crosses indicate the points measured by FCS.
946 Bar: 10 µm. Em-LA or Em-PG molecules move in or out of the confocal volume (white-
947 out cylinder region in blue) at different speeds, as shown in the diagram (right). **(B)**
948 Representative fluorescence fluctuations of Em-LA in DMSO- (green line) and FTI-
949 treated (blue line) of WT and G609G/+ nuclei are plotted by count per second (CPS). **(C)**
950 Diffusion coefficients of fast component (plotted in black) and slow component (plotted
951 in gray) for Em-LA in the cells. **(D)** Representative fluorescence fluctuations of Em-PG
952 in DMSO- (green line) and FTI-treated (blue line) of WT and G609G/+ nuclei are plotted
953 by CPS. **(E)** Diffusion coefficients of fast component (plotted in black) and slow
954 component (plotted in gray) for Em-PG in the cells. **(C** and **E)** Mean ± SEM are indicated
955 on the left to plots; n = 10 cells from two independent experiments; *, P < 0.05 by a
956 Games–Howell test. Percentiles of these component fractions are indicated at the bottom
957 of the graph. N/A, not applicable because of photobleaching.
958
959 Figure 4. **The localization of pre- and mature-LA to the rupture sites in the control**
960 **and Zmpste24-KD WT MEFs treated with DMSO or FTI. (A)** Whole cell lysates from
961 the control and Zmpste24-KD cells treated with DMSO or FTI were probed with anti-
962 LA/C (3A6-4C11) and anti-GAPDH (as loading control). Positions of the size standards
963 are shown on the right. **(B)** The control and shZmpste24 cells treated with DMSO or FTI
964 were immunostained with a combination of anti-pre-LA (7G11) and anti-mature-LA
965 (4A4-A4). Bar: 5 µm. **(C** and **D)** NP/NL ratios of pre-LA (C) and mature-LA (D) in the
966 cells were measured based on immunofluorescence (n = 20 cells from two independent
967 experiments; ***, P < 0.001 by Games–Howell tests for pre-LA and by Welch's t-test for
968 mature-LA). **(E)** 15 to 18 of nuclei in the cells were laser-microirradiated within 10 min
969 and incubated for 60 min, followed by fixation with 4% PFA/0.1% Triton-X 100. The
970 fixed cells were immunostained with a combination of the mature-LA and pre-LA
971 antibodies. Percentiles of the indicated cells with (blue) and without (gray) the
972 localization of LA and pre-LA to NE rupture sites. The numbers of analyzed cells from

973 two independent experiments are indicated in the bar charts. **(C-D)** N/A, not applicable
974 due to below detection limit.
975
976 Figure 5. **Rapid accumulation of LA truncation and PG deletion mutants at the**
977 **rupture sites in LA/C-KO nuclei.** **(A)** Architecture of mEmerald-fused LA-full-length
978 (FL), PG, PG-CSM, L648X, T644X, F627X, S617X, A601X, S575X, LAΔ26, LAΔ26-
979 L648X, LAΔ26-L644X, LAΔ26-L627X, and LC. Terminal amino acids are numbered,
980 and their accumulation dynamics is summarized on the right (+, accumulated at the
981 rupture site; -, not accumulated). **(B** and **C)** The mEmerald-fused LA-FL, PG, PG-CSM,
982 L648X, T644X, F627X, S617X, A601X, S575X and LC were ectopically expressed
983 under the *Lmna* promoter in LA/C-KO cells. **(B)** Representative confocal images of the
984 indicated nuclei. Bar: 5 μm. **(C)** The NP/NL ratios were measured based on mEmerald
985 signals (n = 15-20 cells from two independent experiments; ‡, P<0.001 compared to
986 others except PG-CSM and *, P < 0.05 by a Games–Howell test). **(D** and **E)** Time-lapse
987 images of mEmerald-fused LA-FL, LA mutants, PG, PG deletion mutant and LC were
988 acquired with 10 s intervals for 3 min after the induction of NE rupture by laser-
989 microirradiation, and the relative intensities at the rupture sites are plotted in the graphs.
990 The fluorescence intensities at the rupture sites were measured and normalized to the
991 initial intensities (means ± SEM; n =20 cells from two independent experiments; ***, P
992 < 0.001 from LA-FL by a mixed effect model). **(D)** mEmerald-fused LA-FL, PG, PG-
993 CSM, L648X, T644X, F627X, S617X, A601X, S575X and LC. **(E)** mEmerald-fused LA-
994 FL, LAΔ26, LAΔ26-L648X, LAΔ26-L644X and LAΔ26-L627X. LA-FL and LC are
995 reproduction of D.
996
997 Figure 6. **Schematic diagram of the difference in localization to the rupture sites**
998 **between LA, LC and PG.** LA (magenta) is slowly localized to the rupture sites compared
999 to LC (green) because it contains two LACSs in the specific tail region (top and middle).
1000 PG (yellow) is even slower in localizing to the rupture sites than LA because of the
1001 permanent association with the INM. PG expression also slows the recruitment of LA and
1002 LC to the rupture sites. When the farnesylation of PG is inhibited by FTI treatment, the
1003 localization kinetics becomes similar to that of LA (bottom).

1004 Table S1. **Phenotype characterization of WT and G609G/+ MEFs.**
1005 NLS-sfCherry expressing WT and G609G/+ cells were stained with Hoechst 33342 for
1006 DNA and RFP-Booster Alexa Fluor 568 to enhance the signal of NLS-sfCherry to detect
1007 spontaneous NE rupture. Immunostaining with α-LB1 and α-cGAS antibodies were also
1008 used as NE rupture markers. See Fig. S1 A for the confocal images. P values, Fisher's
1009 exact tests between WT and G609G/+.
1010
1011 Table S2. **Oligonucleotides used in this study.**
1012 See Materials and methods. Oligonucleotides were synthesized by Sigma-Aldrich or
1013 Integrated DNA Technologies (IDT).
1014
1015 Figure S1. **Phenotype characterization, the localization kinetics of LA and PG at the**
1016 **rupture sites in WT and G609G/+ MEFs, and the localization kinetics of LA at the**
1017 **rupture sites in BAF-KD WT MEFs. (A)** The phenotype of heterozygous knock-in
1018 G609G/+ expressing NLS-sfCherry was characterized by immunofluorescence. The cells
1019 were immunostained with anti-LB1 and anti-cGAS, and the DNA was stained with
1020 Hoechst 33342. The fluorescence intensities of NLS-sfCherry are shown with rainbow
1021 color. Asterisk indicates a cell with NE breakdown due to the G2-M transition and were
1022 excluded from the analysis. Misshapen, NE-ruptured, LB1-mis-localized and cGAS-
1023 accumulated nuclei are indicated with magenta arrowheads. **(B)** Representative confocal
1024 images of the nuclei. Magnified views of the indicated areas by orange boxes are shown
1025 (bottom of each row). The cells were fixed within 0-10 min (top), 30-40 min (middle) and
1026 120-130 min (bottom) after the induction of NE rupture by laser microirradiation,
1027 followed by fixation with 4% PFA/0.1% Triton-X 100. The fixed cells were
1028 immunostained with anti-LA (4A58) and anti-PG. The rupture sites are indicated with
1029 yellow arrowheads (bottom of each row). Bars: 5 μm (top of each row) and 2 μm (bottom
1030 of each row). **(C)** Whole cell lysates from WT cells expressing shRNAs for the control
1031 (Scramble) or two shRNAs (shBAF #1 and #2) were probed with anti-BANF1/BAF and
1032 anti-GAPDH (as loading control) for immunostaining. Positions of the size standards are
1033 shown on the right. **(D** and **F)** 15 to 19 of the indicated cells were laser-microirradiated
1034 within 10 min and incubated for 60 min, followed by fixation with 4% PFA/0.1% Triton-
1035 X 100. The fixed cells were immunostained with the LA and BAF antibodies. **(D)**
1036 Representative confocal images of nuclei with (blue arrowheads) or without (magenta
1037 arrowheads) the localization of LA to the rupture sites. Bar: 40 μm. **(E)** Percentiles of
1038 cells with (blue) and without (gray) the localization of LA. The numbers of analyzed cells
1039 from two independent experiments are indicated in the bar charts.
1040
1041 Figure S2. **Accumulation kinetics of LC at the rupture sites in WT and G609G/+**
1042 **MEFs. (A)** Protein architecture of LA, LC and PG with sfGFP-DARPin-LA6. The

1043 summary of their accumulation at the rupture sites is indicated on the right (+,
1044 accumulated at the rupture site; -, not accumulated). The structural image of sfGFP-
1045 DARPin-LA6 was predicted by AlphaFold2 (79) and edited by the PyMOL (Schrödinger).
1046 **(B** and **C)** Time-lapse images of sfGFP-DARPin-LA6 expressed in WT and G609G/+
1047 cells were acquired with 10 s intervals for 3 min after the induction of NE rupture by
1048 laser-microirradiation, and the relative intensities are plotted in the graph. **(B)** The
1049 dynamics of the sfGFP-DARPin-LA6 in response to NE rupture in the cells. Magnified
1050 views of the areas indicated by orange boxes are shown (the second to fifth columns). A
1051 2-μm diameter spot at the NE was laser-microirradiated to induce NE rupture (yellow
1052 arrowheads). Bars: 5 μm (the first column) and 2 μm (the second to fifth columns). **(C)**
1053 The fluorescence intensities at the rupture sites were measured and normalized to the
1054 initial intensities (means ± SEM; n = 20 cells from two independent experiments; ***, P
1055 < 0.001 from WT by a mixed effect model).
1056
1057 Figure S3. **Establishment of knock-in cells expressing mEmerald-fused LA, PG and**
1058 **LC under the *Lmna* promoter for FCS measurements.** The DNA sequences of
1059 mEmerald-LC, mEmerald-LA and mEmerald-PG with the endogenous *Lmna* promotor
1060 were knocked-in to the *Rosa26* locus in WT and G609G/+ cells. **(A)** The schematic
1061 diagram of linearized pLmna-Em-LA-R26Neo, pLmna-Em-PG-R26Neo and pLmna-
1062 Em-LC-R26Neo knock-in vectors. **(B)** Whole cell lysates from the knocked-in cells with
1063 pLmna-Em-LA-R26Neo, pLmna-Em-PG-R26Neo and pLmna-Em-LC-R26Neo were
1064 probed with anti-LA/C (3A6-4C11) and anti-β-actin (as loading control) for
1065 immunostaining. Positions of the size standards are shown on the right. **(C-E)** The
1066 diffusion fractions and coefficients of mEmerald-LC (Em-LC) in WT and G609G/+
1067 nuclei were measured by FCS. **(C)** A representative confocal image of a WT nucleus with
1068 mEmerald-LC before FCS measurements (top). The yellow crosses indicate the points
1069 measured by FCS. Bar: 10 μm. Em-LC molecules move in or out of the confocal volume
1070 (white-out cylinder region in blue) at different speeds, as shown in the diagram (bottom).
1071 **(D)** Diffusion coefficient of fast component (plotted in black) and slow component
1072 (plotted in gray) for Em-LC in the cells. Mean ± SEM are indicated on the left to plots; n
1073 = 10 cells from two independent experiments; ***, P < 0.001 by a Welch's t-test.
1074 Percentiles of these components are indicated at the bottom of the graph.
1075
1076 Figure S4. **Short-term localization of LA and PG to the rupture sites in DMSO or**
1077 **FTI-treated WT and G609G/+ nuclei.** 14 to 15 of nuclei in the cells were laser-
1078 microirradiated within 10 min, followed by fixation with 4% PFA/0.1% Triton-X 100.
1079 The fixed cells were immunostained with a combination of the LA and PG antibodies.
1080 Percentiles of the cells with (blue) and without (gray) the localization of LA and PG at
1081 the rupture sites. The numbers of analyzed cells from two independent experiments are

1082 indicated in the bar charts. The number of the cells in which LA and PG were localized
1083 to the rupture sites are indicated at the bottom of the graph.
1084
1085 Figure S5. **The immunoblotting of FTI-treated WT and G609G/+ knocked-in MEFs.**
1086 Whole cell lysates from the knocked-in cells with pLmna-Em-LA-R26Neo (Em-LA) and
1087 pLmna-Em-PG-R26Neo (Em-PG) treated with DMSO or FTI were probed with anti-
1088 LA/C (3A6-4C11) and anti-GAPDH (as loading control) for immunostaining. Positions
1089 of the size standards are shown on the right.
1090
1091 Figure S6. **The localization kinetics at the rupture sites in the control and Zmpste24-**
1092 **KD WT MEFs. (A)** Whole cell lysates from WT cells expressing Scramble for the
1093 control or shZmpste24 for Zmpste24-KD were probed with anti-pre-LA (7G11), anti-
1094 LA/C (3A6-4C11) and anti-GAPDH (as loading control) for immunobloting. Positions of
1095 the size standards are shown on the right. **(B** and **C)** The cells were immunostained with
1096 anti-LA (4A58) and the pre-LA (7G11) antibody. **(B**) Representative confocal images of
1097 the nuclei. Bar: 5 μm. **(C)** NP/NL ratios of LA and pre-LA were measured based on
1098 immunofluorescence (n = 20 cells from two independent experiments). **(D** and **E)** 18 of
1099 nuclei in the cells were laser-microirradiated within 10 min and incubated for 60 min,
1100 followed by fixation with 4% PFA/0.1% Triton-X 100. The fixed cells were
1101 immunostained with the LA and pre-LA antibodies. **(D)** Representative confocal images
1102 of the nuclei with (blue arrowheads) or without (magenta arrowheads) the localization of
1103 LA and pre-LA to the rupture sites. Bar: 40 μm. **(E)** Percentiles of the cells with (blue)
1104 and without (gray) the localization of LA and pre-LA. The numbers of analyzed cells
1105 from two independent experiments are indicated in the bar charts.
1106
1107 Figure S7. **Accumulation kinetics of LA and PG mutants at the rupture sites in LA/C-**
1108 **KO MEFs. (A)** Amino acid sequences of LA- (blue) or LC-specific (red) regions from
1109 *Homo sapiens* and *Mus musculus*. The amino acid homology is indicated as bars and a
1110 gap is introduced between residue A600 and A601 in *Mus musculus* to maximize the
1111 homology. **(B)** Dynamics of the mEmerald-LA-S575X and A601X in response to NE
1112 rupture in LA/C-KO MEFs. **(C)** Representative images of mEmerald-LA-full-length (FL),
1113 LA-FL without LACS1 (LAΔ26), LAΔ26-L648X, LAΔ26-T644X, LAΔ26-F627X, and
1114 mEmerald-LC in LA/C-KO MEFs transfected for 2 d. Bar: 5 μm. **(D)** Fluorescence
1115 intensities in the NP to the NL ratio of mEmerald-LA mutants and mEmerald-LC, as
1116 control, were measured (n = 14-20 cells from two independent experiments; ***, P <
1117 0.001 by a Games–Howell test). (**C** and **D**) LA-FL and LC are reproduction of Fig. 5 B
1118 and C. **(E)** Dynamics of the mEmerald-LAΔ26-F627X and LAΔ26-T644X in response to
1119 NE rupture in LA/C-KO MEFs. **(B** and **E)** Magnified views of the indicated areas by
1120 orange boxes are shown (the second to fifth columns). A 2-μm diameter spot was laser-

1121 microirradiated to induce NE rupture (yellow arrowheads). Bars: 5 μm (the first column)
1122 and 2 μm (the second to fifth columns).

Fig. 1

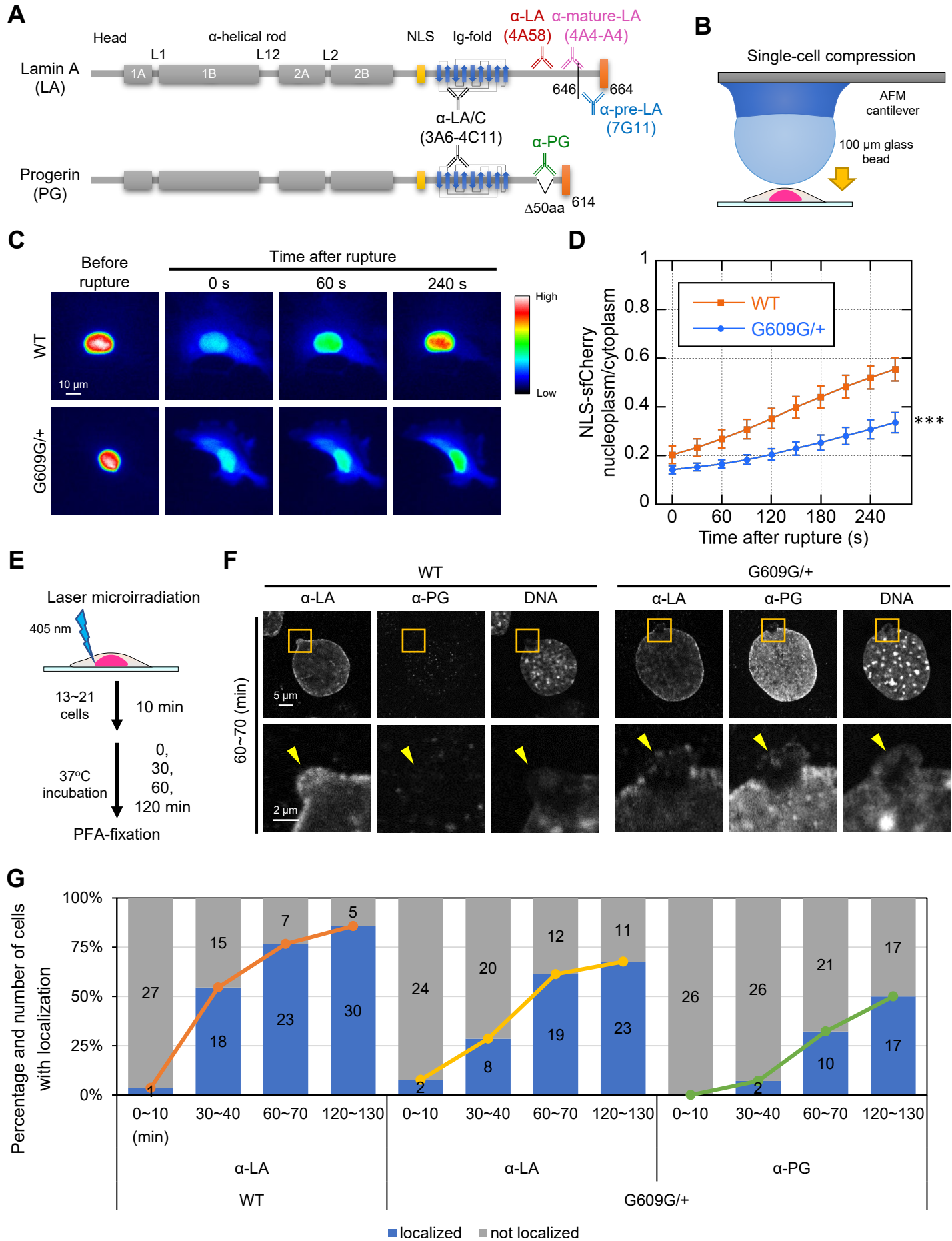
A
Head
α-helical rod
L1
L12
L2
NLS
Ig-fold
α-LA (4A58)
α-mature-LA (4A4-A4)
Lamin A (LA)
1A
1B
2A
2B
646
664
α-pre-LA (7G11)
α-LA/C (3A6-4C11)
α-PG
Progerin (PG)
Δ50aa
614
B
Single-cell compression
AFM cantilever
100 μm glass bead
C
Before rupture
Time after rupture
0 s
60 s
240 s
WT
G609G/+
10 μm
High
Low
D
NLS-sfCherry nucleoplasm/cytoplasm
WT
G609G/+
***
Time after rupture (s)
E
Laser microirradiation
405 nm
13~21 cells
10 min
37°C incubation
0, 30, 60, 120 min
PFA-fixation
F
WT
G609G/+
α-LA
α-PG
DNA
60~70 (min)
5 μm
2 μm
G
Percentage and number of cells with localization
100%
75%
50%
25%
0%
0~10 (min)
30~40
60~70
120~130
α-LA
α-PG
WT
G609G/+
localized
not localized

Fig. 2

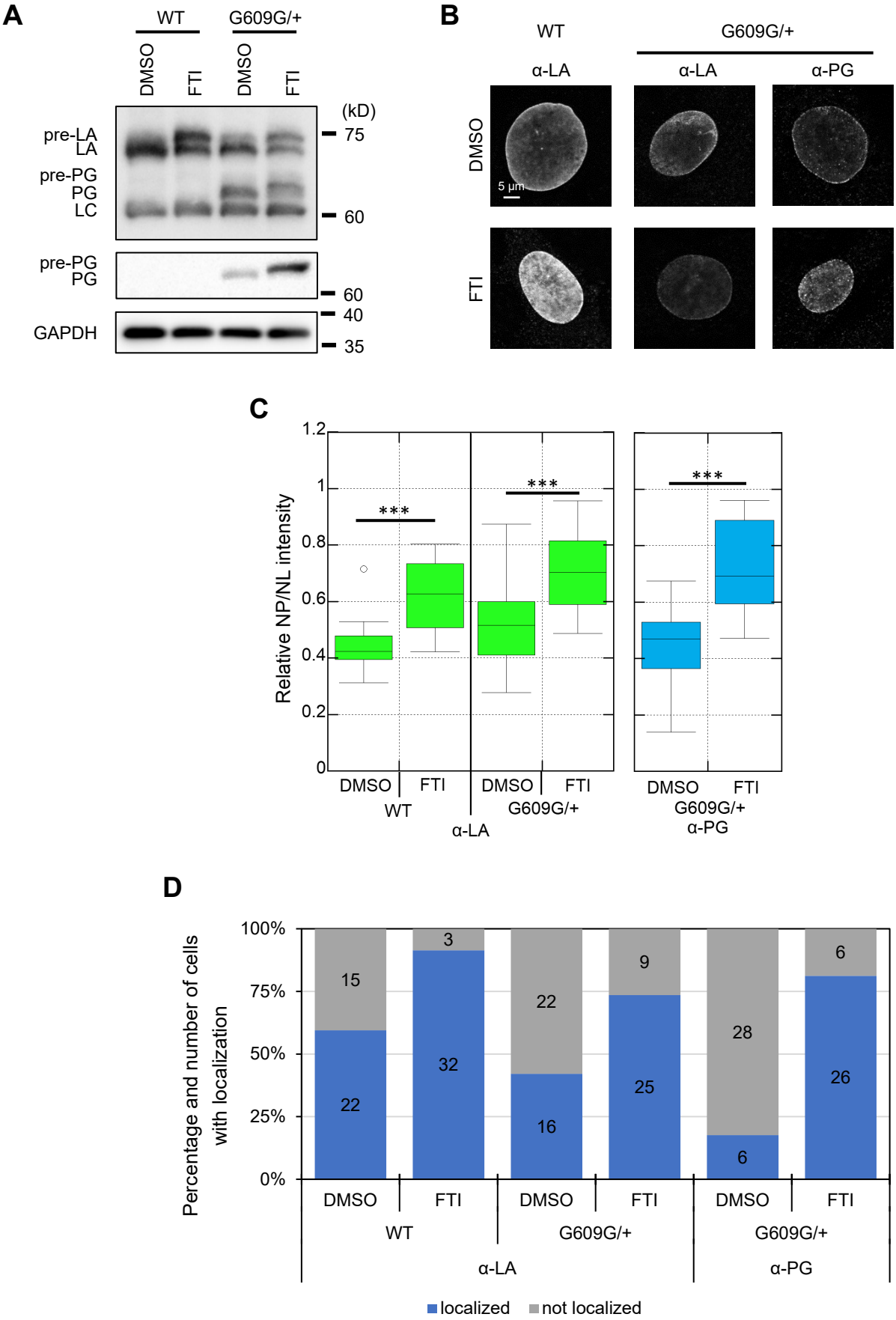
A
WT
G609G/+
DMSO
FTI
DMSO
FTI
(kD)
pre-LA
LA
pre-PG
PG
LC
75
60
pre-PG
PG
60
40
GAPDH
35
B
WT
G609G/+
α-LA
α-LA
α-PG
DMSO
FTI
5 μm
C
Relative NP/NL intensity
1.2
1
0.8
0.6
0.4
0.2
0
***
***
***
DMSO
FTI
DMSO
FTI
DMSO
FTI
WT
G609G/+
G609G/+
α-LA
α-PG
D
Percentage and number of cells with localization
100%
75%
50%
25%
0%
15
22
3
32
22
16
9
25
28
6
6
26
DMSO
FTI
DMSO
FTI
DMSO
FTI
WT
G609G/+
G609G/+
α-LA
α-PG
localized
not localized

Fig. 3

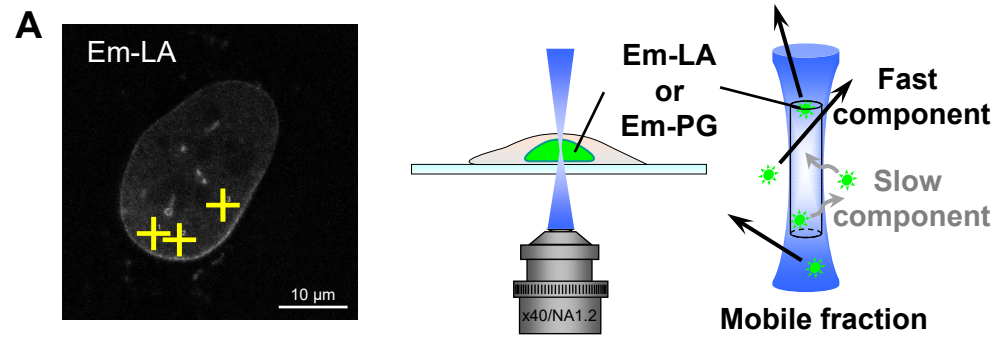

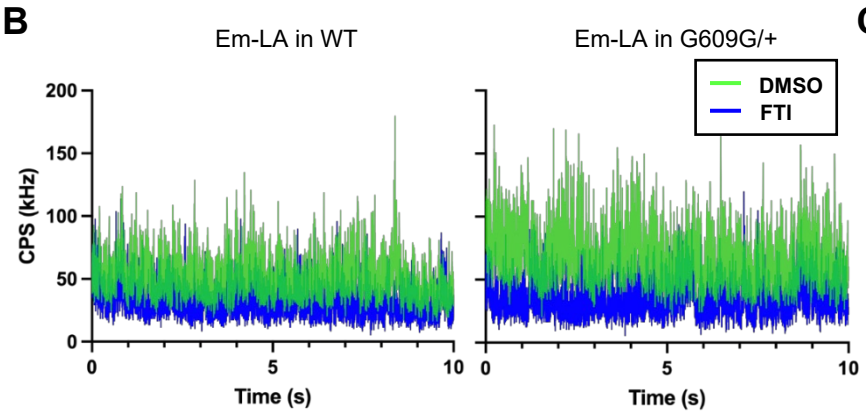

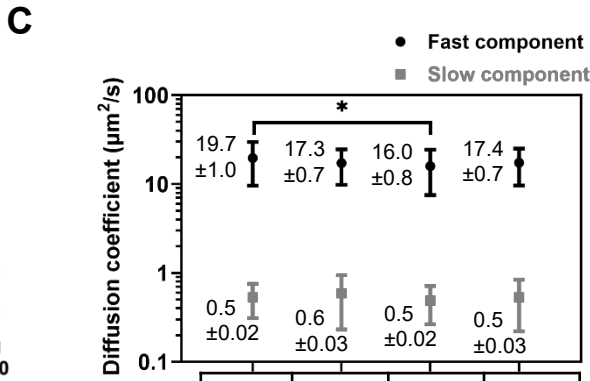

		WT DMSO	WT FTI	G609G/+ DMSO	G609G/+ FTI
Component fraction (%)	Fast	41.7	48.7	44	49.2
	Slow	58.3	51.3	56	50.8

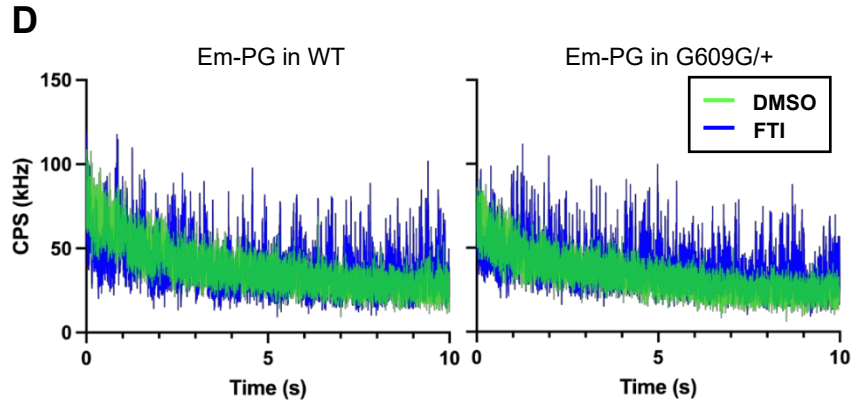

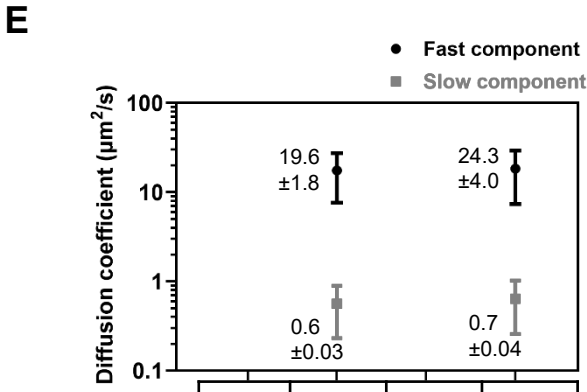

		WT DMSO	WT FTI	G609G/+ DMSO	G609G/+ FTI
Component fraction (%)	Fast	N/A	38.3	N/A	42.2
	Slow	N/A	61.7	N/A	57.8

Fig. 4

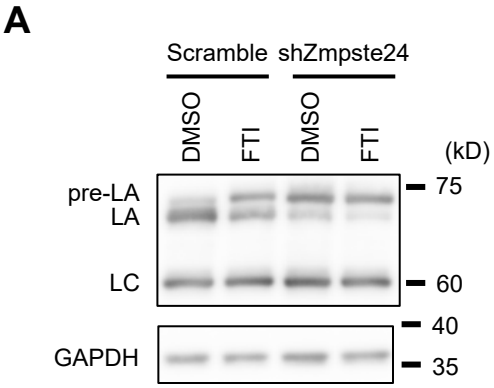
A
Scramble
shZmpste24
DMSO
FTI
DMSO
FTI
(kD)
pre-LA
LA
LC
GAPDH
75
60
40
35

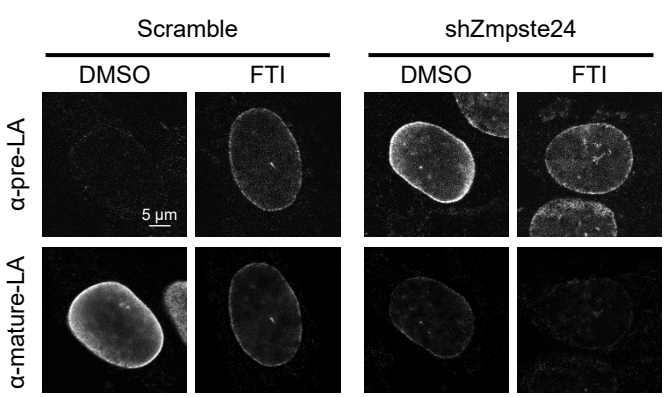
B
Scramble
shZmpste24
DMSO
FTI
DMSO
FTI
α-pre-LA
α-mature-LA
5 μm

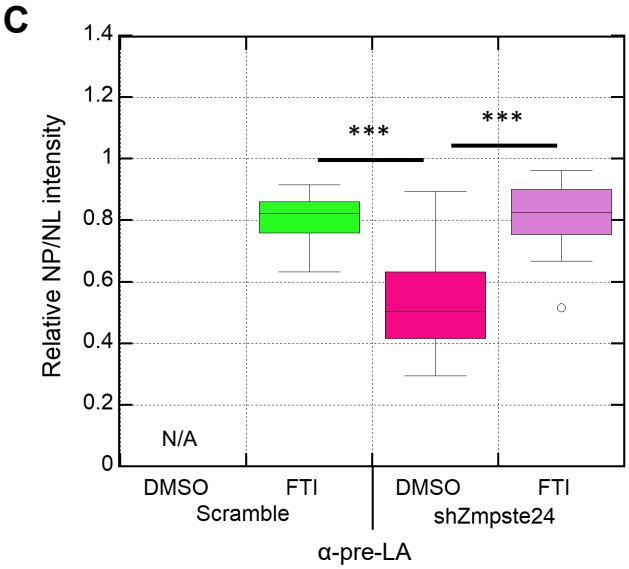
C
Relative NP/NL intensity
1.4
1.2
1
0.8
0.6
0.4
0.2
0
***
***
N/A
DMSO
FTI
DMSO
FTI
Scramble
shZmpste24
α-pre-LA

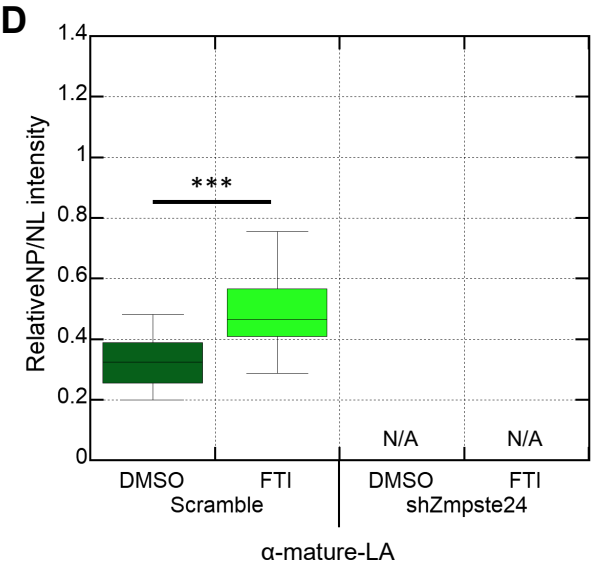
D
RelativeNP/NL intensity
1.4
1.2
1
0.8
0.6
0.4
0.2
0
***
N/A
N/A
DMSO
FTI
DMSO
FTI
Scramble
shZmpste24
α-mature-LA

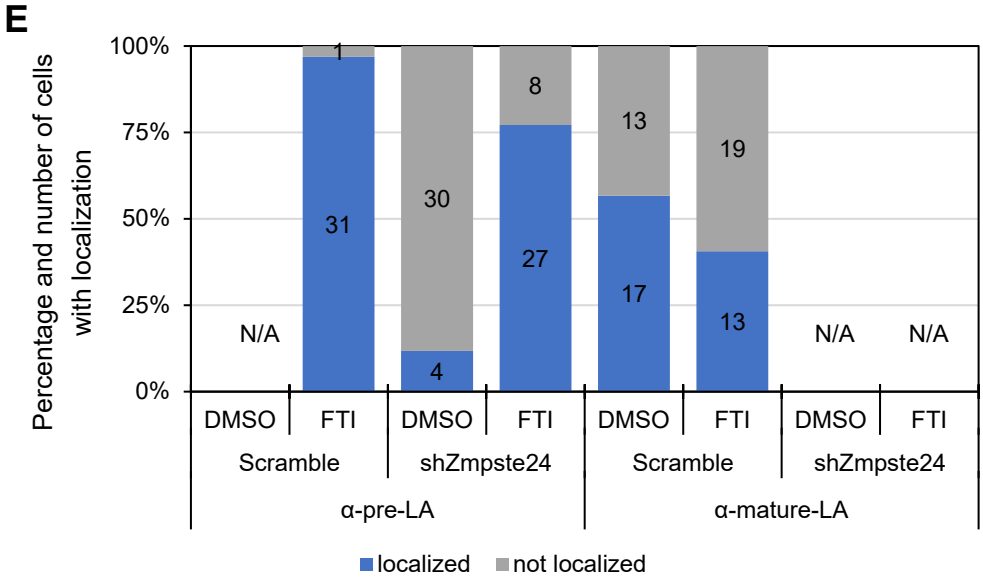
E
Percentage and number of cells with localization
100%
75%
50%
25%
0%
N/A
1
31
30
4
8
27
13
17
19
13
N/A
N/A
DMSO
FTI
DMSO
FTI
DMSO
FTI
DMSO
FTI
Scramble
shZmpste24
Scramble
shZmpste24
α-pre-LA
α-mature-LA
localized
not localized

Fig. 5

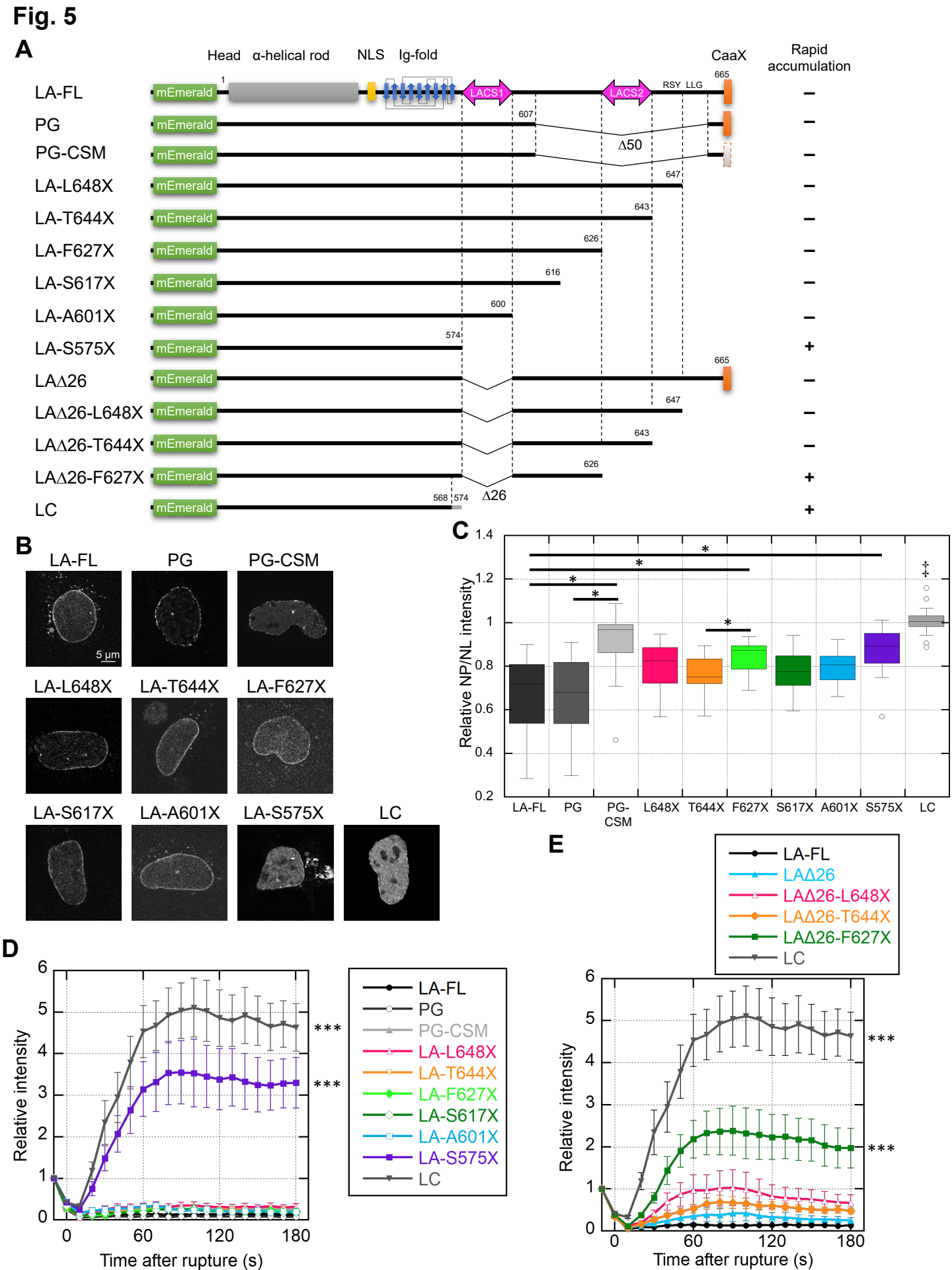
A
Head
α-helical rod
NLS
Ig-fold
CaaX
Rapid accumulation
LA-FL
PG
PG-CSM
LA-L648X
LA-T644X
LA-F627X
LA-S617X
LA-A601X
LA-S575X
LAΔ26
LAΔ26-L648X
LAΔ26-T644X
LAΔ26-F627X
LC
mEmerald
LACS1
LACS2
RSY LLG
Δ50
Δ26
B
5 μm
C
Relative NP/NL intensity
D
Relative intensity
Time after rupture (s)
E
Relative intensity
Time after rupture (s)

Fig. 6

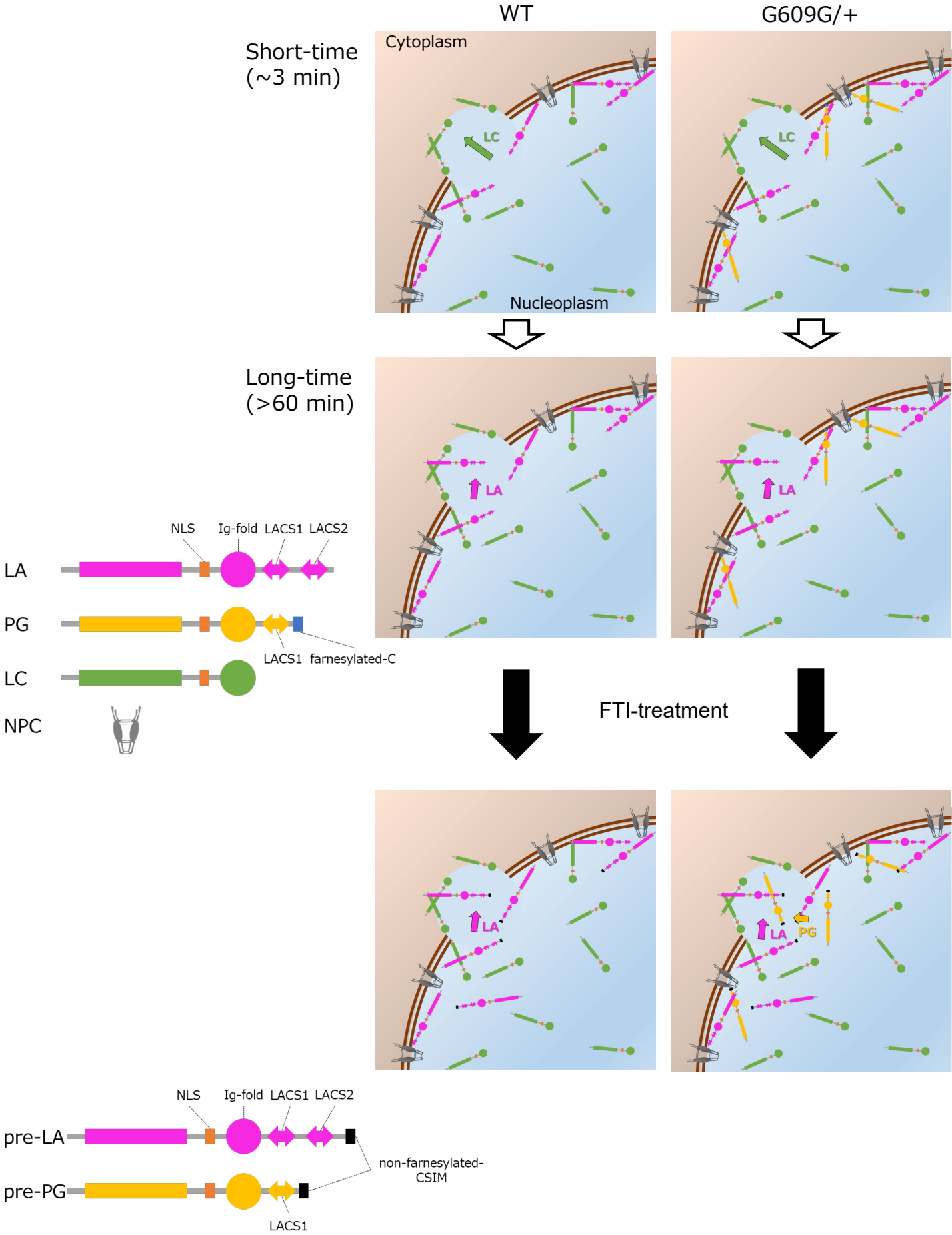
WT
G609G/+
Short-time
(~3 min)
Cytoplasm
LC
Nucleoplasm
Long-time
(>60 min)
LA
NLS
Ig-fold
LACS1
LACS2
LA
PG
LACS1
farnesylated-C
LC
NPC
FTI-treatment
LA
LA
PG
NLS
Ig-fold
LACS1
LACS2
pre-LA
pre-PG
non-farnesylated-
CSIM
LACS1

Table S1. Phenotype characterization of WT and G609G/+ MEFs

	WT (n = 118 cells, 129 nuclei)	G609G/+ (n = 116 cells, 131 nuclei)	P value
DNA			0.465
normal	122 (94.6%)	120 (91.6%)	
mis-shapen	7 (5.4%)	11 (8.4%)	
NLS-sfCherry			0.102
nuclear-localized	110 (93.2%)	114 (98.3%)	
ruptured	8 (6.8%)	2 (1.7%)	
α-LB1			0.212
normal distributed	125 (96.9%)	130 (99.2%)	
mis-localized	4 (3.1%)	1 (0.8%)	
α-cGAS			1
not accumulated	129 (100%)	131 (100%)	
accumulated	0 (0%)	0 (0%)	

NLS-sfCherry expressing WT and G609G/+ cells were stained with Hoechst 33342 for DNA and RFP-Booster Alexa Fluor 568 to enhance the signal of NLS-sfCherry to detect spontaneous NE rupture. Immunostaining with α-LB1 and α-cGAS antibodies were also used as NE rupture markers. See Fig. S1 A for the confocal images. P values, Fisher's exact tests between WT and G609G/+.

Table S2. Oligonucleotides used in this study

No.	Name	Sequence (5' to 3')
1	shSte24#1-TRCN0000366641_S	CCGGCTGGATGCTCTTCCGGTTATTCTCGAGAATAACCGGAAGAGCATCCAGTTTTTG
2	shSte24#1-TRCN0000366641_AS	AATTCAAAAACTGGATGCTCTTCCGGTTATTCTCGAGAATAACCGGAAGAGCATCCAG
3	shBanf1#1-TRCN0000124958_Fw	CCGGTGGCCAGTTTCTGGTGCTAAACTCGAGTTTAGCACCAGAAACTGGCCATTTTTG
4	shBanf1#1-TRCN0000124958_Rv	AATTCAAAAATGGCCAGTTTCTGGTGCTAAACTCGAGTTTAGCACCAGAAACTGGCCA
5	shBanf1#2-TRCN0000124955_Fw	CCGGGACAAGGCTTATGTGGTCCTTCTCGAGAAGGACCACATAAGCCTTGTCTTTTTG
6	shBanf1#2-TRCN0000124955_Rv	AATTCAAAAAGACAAGGCTTATGTGGTCCTTCTCGAGAAGGACCACATAAGCCTTGTC
7	pX459V2-Fw	GAATTCTAACTAGAGCTCGCTGATCAGCCTCG
8	pX459V2-Rv	TGGGCCAGGATTCTCCTCGACGTCAC
9	if_mCherry_Fw	GAGAATCCTGGCCCAATGGTGAGCAAGGGCGAGGAGG
10	if_mCherry_Rv	CTCTAGTTAGAATTCTCACTTGTACAGCTCGTCCATGCCGCCGG
11	sgRosa26-1_s	CACCGACTCCAGTCTTTCTAGAAGA
12	sgRosa26-1_as	AAACTCTTCTAGAAAGACTGGAGTC
13	if_LA promoter_Fw	ATGCATTAGTTATTAATTGCCTCGAAAAACCAAAAAAAG
14	if_LA promoter_Rv	GACCGGTAGCGCTAGCCCGCTGTGACGGGGTCTCCATG
15	if_mLA_Fw	ATGGAGACCCCGTCACAGCGG
16	if_mLA_Rv	AACCGGTAGCGCTAGCCATGATGCTGCAGTTCTGGG
17	mLA-to-PG_Fw	CAGAGCTCCCAGAACTGCAGC
18	mLA-to-PG_Rv	TCTGGGAGCTCTGGGCTCCCGCTCCACCG
19	mLA-L648X_Fw (mature)	CACCCGCTCCTACTAGCTGGGCAACTCC
20	mLA-L648X_Rv (mature)	GGAGTTGCCCAGCTAGTAGGAGCGGGTG
21	mLA-T644X_Fw	GACAACCTAGTCTAACGCTCCTACCTC
22	mLA-T644X_Rv	GAGGTAGGAGCGTTAGACTAGGTTGTC
23	mLA-F627X_Fw	GTCACTCGAAGCTGACGCAGTGTGGGG
24	mLA-F627X_Rv	CCCCACACTGCGTCAGCTTCGAGTGAC
25	mLA-S617X_Fw	CCTCTGGCTCTTGAGCCTCCAGTGTC
26	mLA-S617X_Rv	GACACTGGAGGCTCAAGAGCCAGAGG
27	mLA-A601X_Fw	GCTGACAAGGCTTGAGGTGGAGCGGGAG
28	mLA-A601X_R2	CTCCCGCTCCACCTCAAGCCTTGTCAGCAG
29	mLA-S575X_Fw	CACTGCAGCGGCTAGGGGGACCCCGC
30	mLA-S575X_Rv	GCGGGGTCCCCCTAGCCGCTGCAGTG
31	if_mLA-del575-600_Fw	CAGCGGCGCCGGTGGAGCGGGAGCCC
32	if_mLA-del575-600_Rv	CCACCGGCGCCGCTGCAGTGGGAACCAC
33	if_Rosa26L-mLA_Fw	GTCTTTCTAGCCTTAATTAATGCCTCGAAAAACCAAAA
34	if_mLA-bGHpA-Rv	GAGGTCGACCAATTGTTACATGATGCTGCAGTTCTG
35	if_mLA-CSM-bGHpA-Rv	GAGGTCGACCAATTGTTACATGCTGCAGTTCTGGGAGCT
36	if_bGHpA_Fw	CAATTGGTCGACCTCGACCTCGACTG
37	if_Rosa26R-bGHpA_Rv	GCGGCCGCCGCGCCCACGCGTTCCCCAGCATGCC
38	if_Nsi-BGHpA_Fw	GGCAGCCGCCGCTGAATGCATCAATTGGTCGACCTCGACCTCGACTGT
39	if_mLA-to-mLC_Rv	TCAGCGGCGGCTGCCACTCACACGGTGGTGATGGAGGAGCTCTTCT

See Materials and methods. Oligonucleotides were synthesized by Sigma-Aldrich or Integrated DNA Technologies (IDT).

Fig. S1

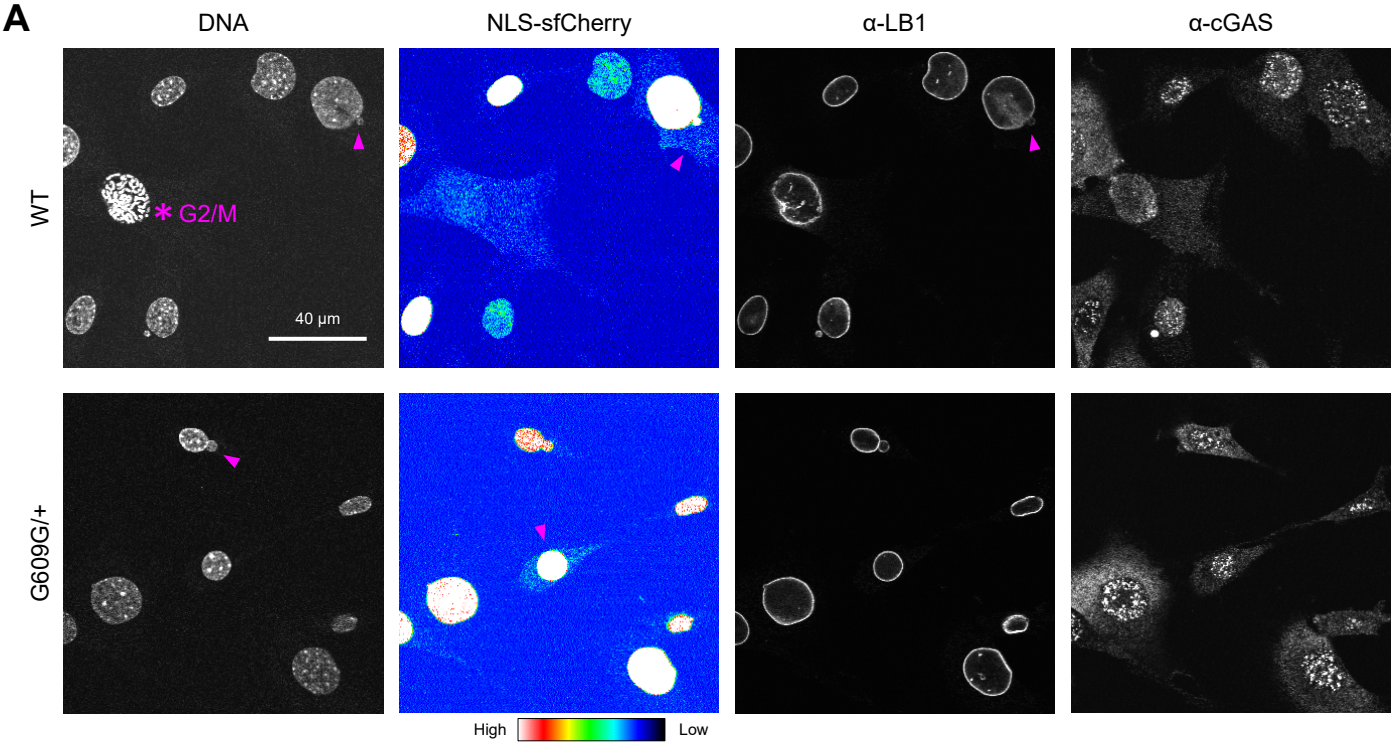
A
DNA
NLS-sfCherry
α-LB1
α-cGAS
WT
G609G/+
* G2/M
40 μm
High
Low

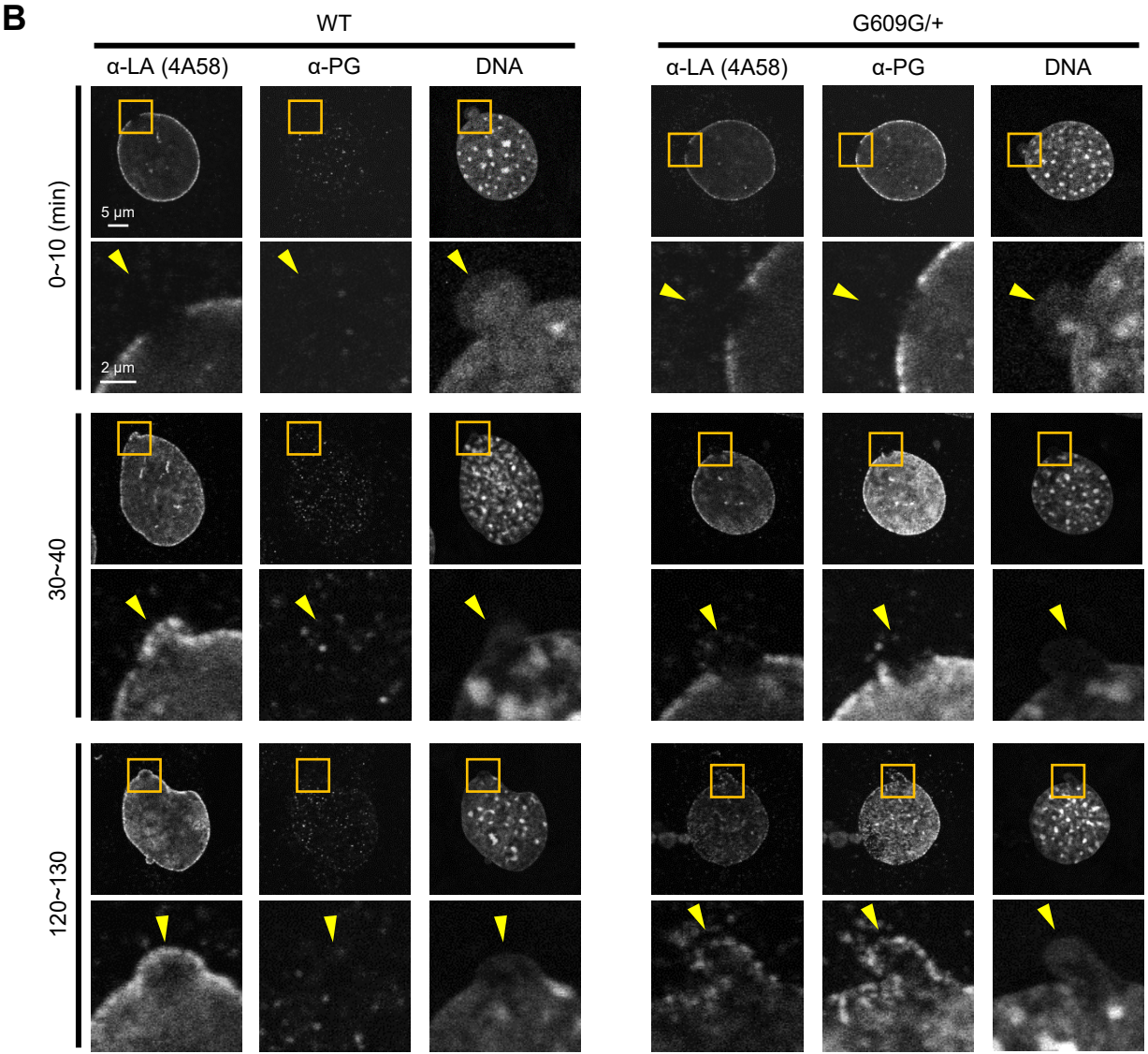
B
WT
G609G/+
α-LA (4A58)
α-PG
DNA
0~10 (min)
30~40
120~130
5 μm
2 μm

Fig. S1

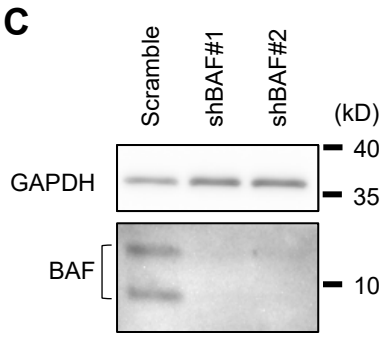
C
Scramble
shBAF#1
shBAF#2
(kD)
40
35
10
GAPDH
BAF

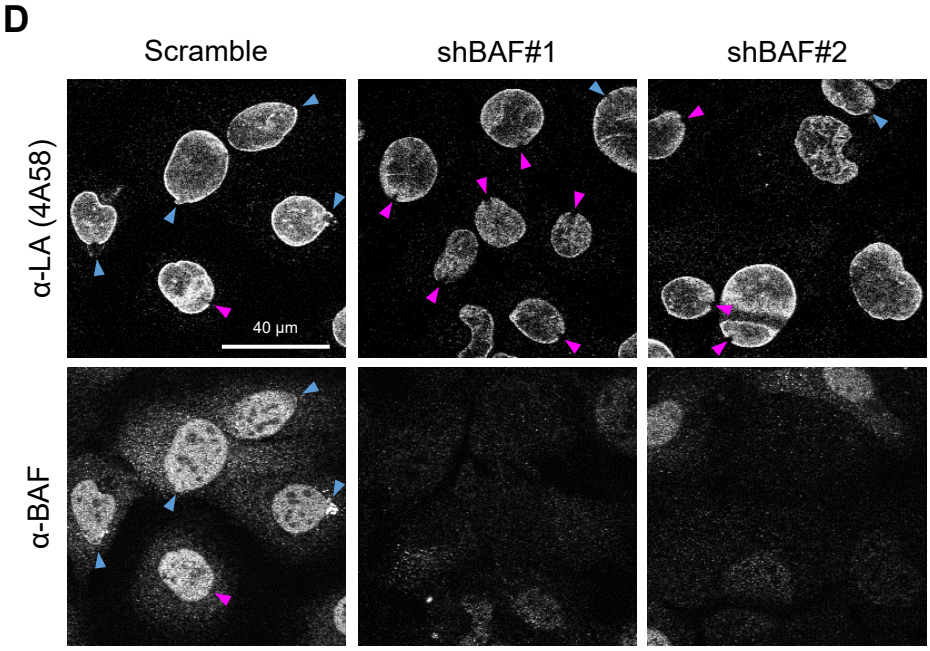
D
Scramble
shBAF#1
shBAF#2
α-LA (4A58)
α-BAF
40 μm

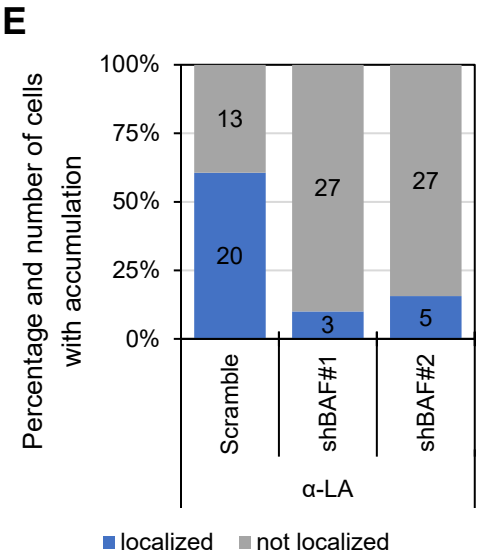
E
Percentage and number of cells with accumulation
100%
75%
50%
25%
0%
13
20
27
3
27
5
Scramble
shBAF#1
shBAF#2
α-LA
localized
not localized

Fig. S2

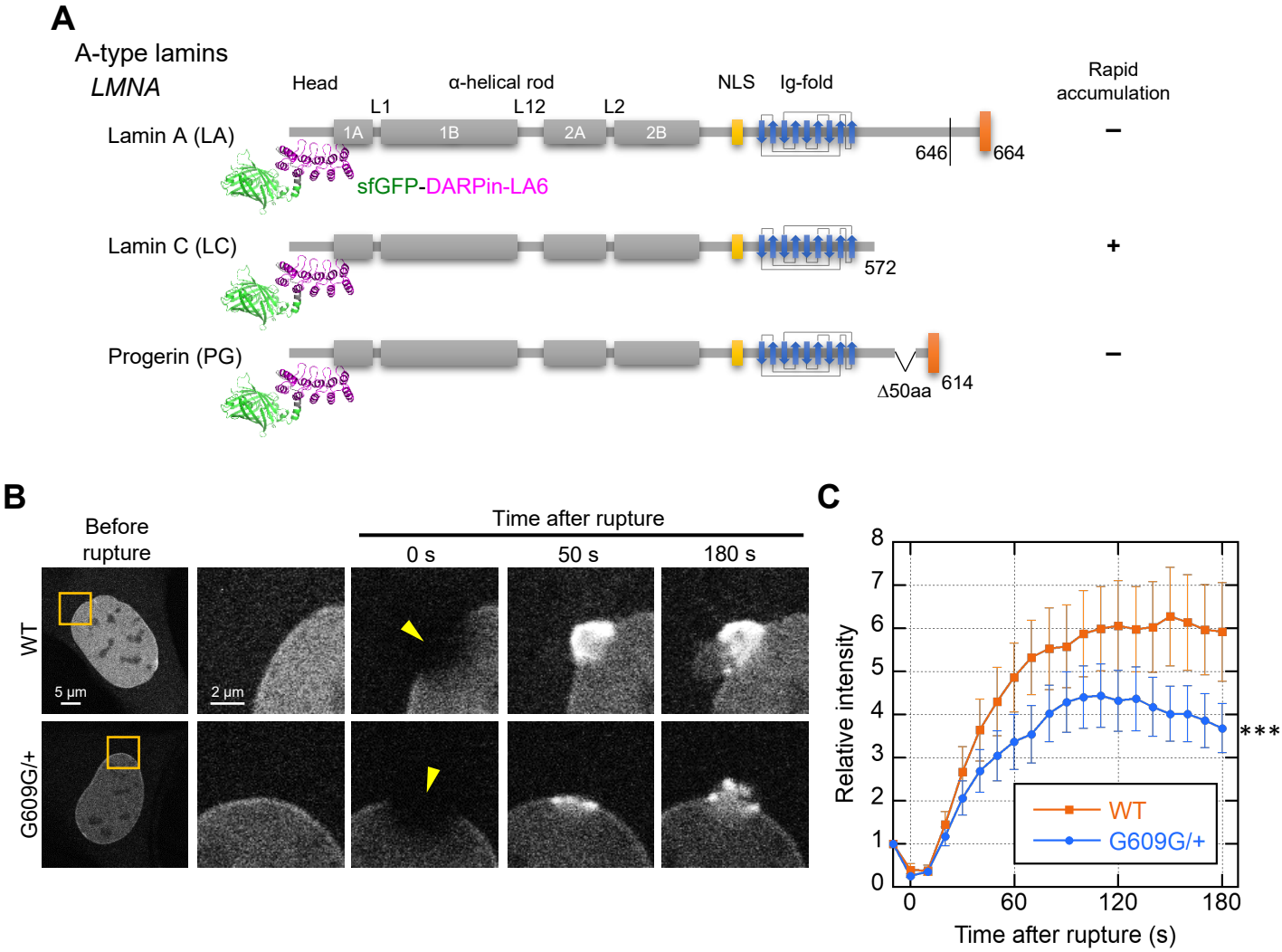
A
A-type lamins
LMNA
Head
α-helical rod
NLS
Ig-fold
Rapid accumulation
L1
L12
L2
1A
1B
2A
2B
Lamin A (LA)
646
664
−
sfGFP-DARPin-LA6
Lamin C (LC)
572
+
Progerin (PG)
Δ50aa
614
−
B
Before rupture
Time after rupture
0 s
50 s
180 s
WT
G609G/+
5 μm
2 μm
C
Relative intensity
Time after rupture (s)
WT
G609G/+
***

Fig. S3

A

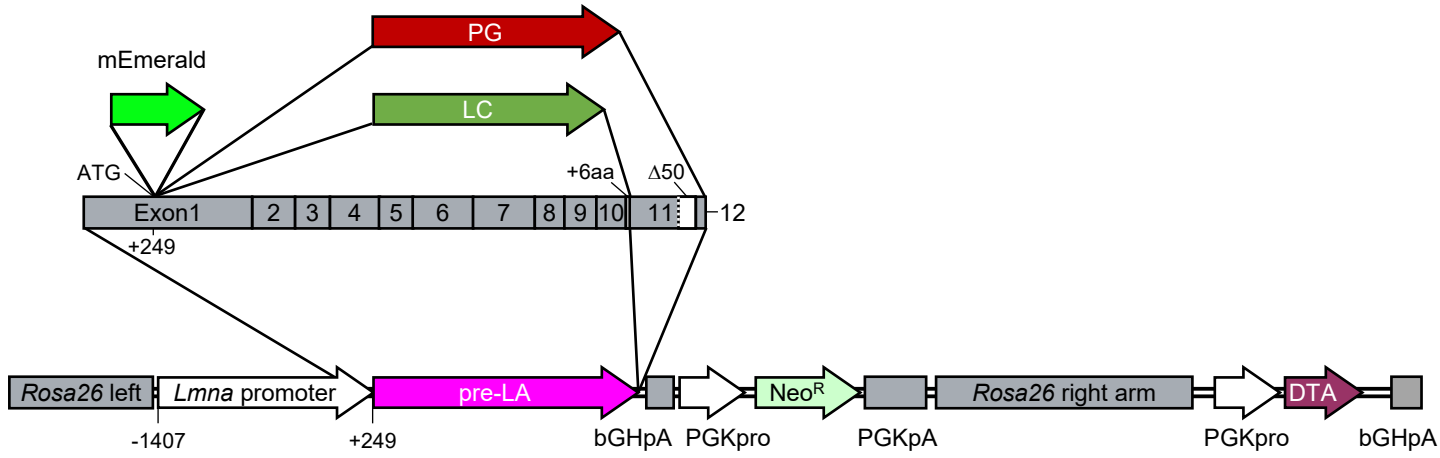

B

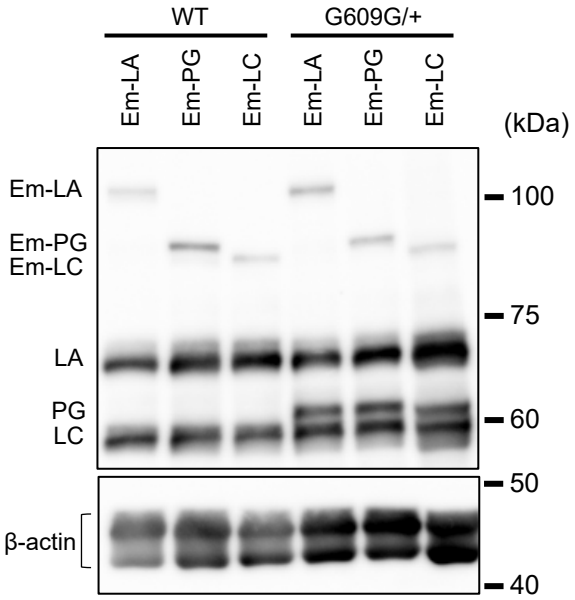

C

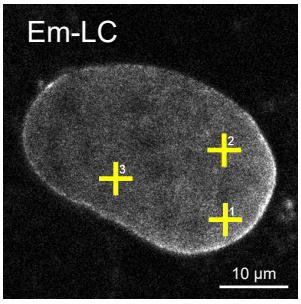

D

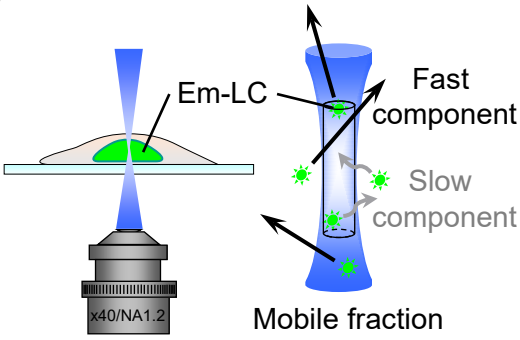

E

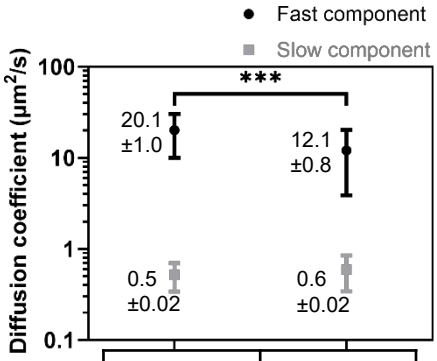

		WT	G609G/+
Component fraction (%)	Fast	37.8	45.0
	Slow	62.2	55.0

Fig. S4

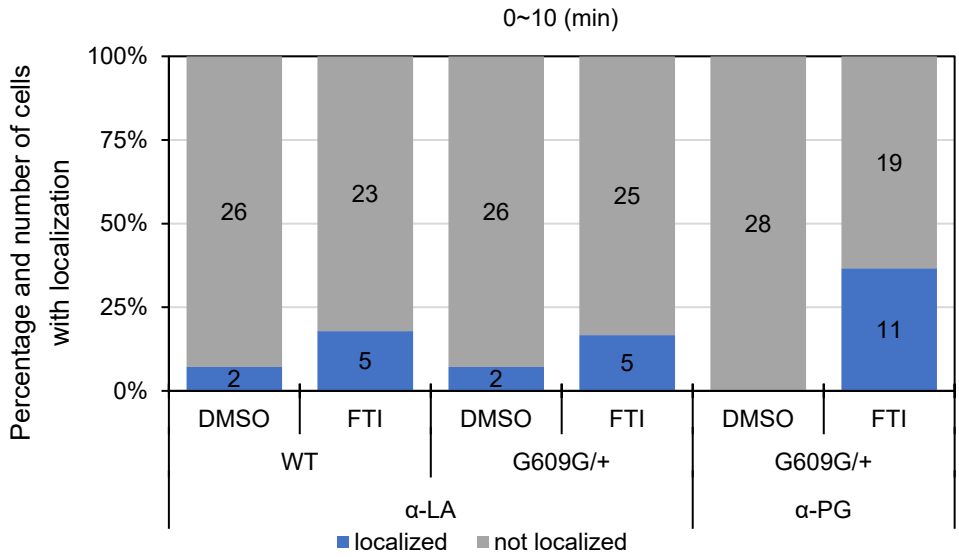

0-5min localized	1	2	0	0	0	0
5-10min localized	1	3	2	5	0	11
not localized	26	23	26	25	28	19

Fig. S5

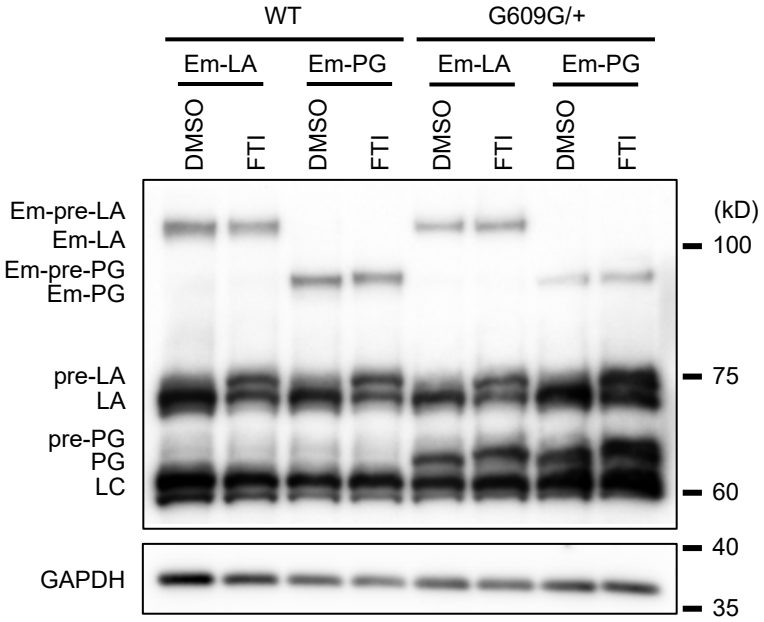
WT
G609G/+
Em-LA
Em-PG
Em-LA
Em-PG
DMSO
FTI
DMSO
FTI
DMSO
FTI
DMSO
FTI
Em-pre-LA
Em-LA
Em-pre-PG
Em-PG
pre-LA
LA
pre-PG
PG
LC
GAPDH
(kD)
100
75
60
40
35

Fig. S6

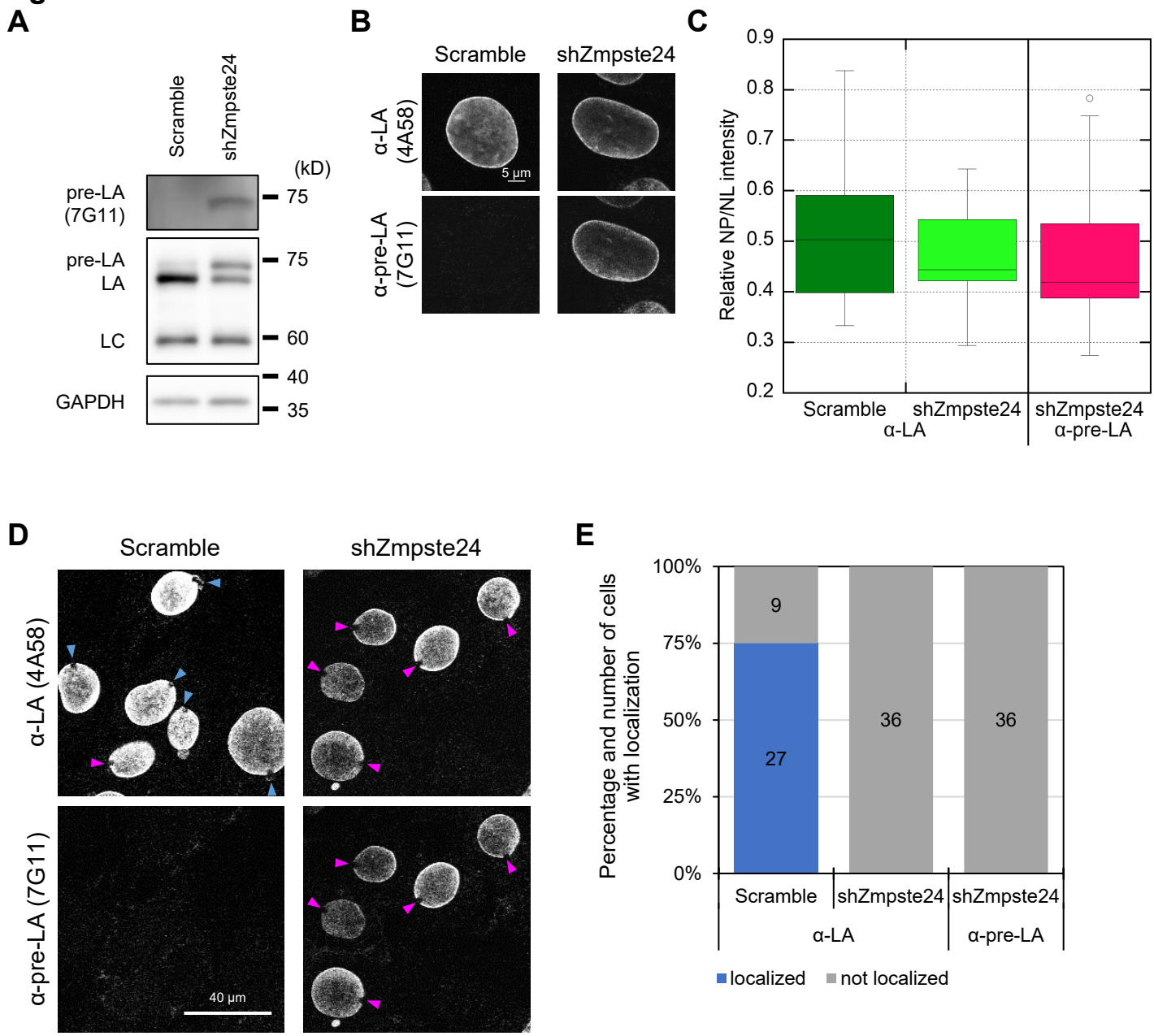
A
Scramble
shZmpste24
(kD)
pre-LA
(7G11)
75
pre-LA
LA
75
LC
60
40
GAPDH
35
B
Scramble
shZmpste24
α-LA
(4A58)
5 μm
α-pre-LA
(7G11)
C
Relative NP/NL intensity
0.9
0.8
0.7
0.6
0.5
0.4
0.3
0.2
Scramble
shZmpste24
α-LA
shZmpste24
α-pre-LA
D
Scramble
shZmpste24
α-LA (4A58)
α-pre-LA (7G11)
40 μm
E
Percentage and number of cells with localization
100%
75%
50%
25%
0%
9
27
36
36
Scramble
shZmpste24
shZmpste24
α-LA
α-pre-LA
localized
not localized

Fig. S7

A

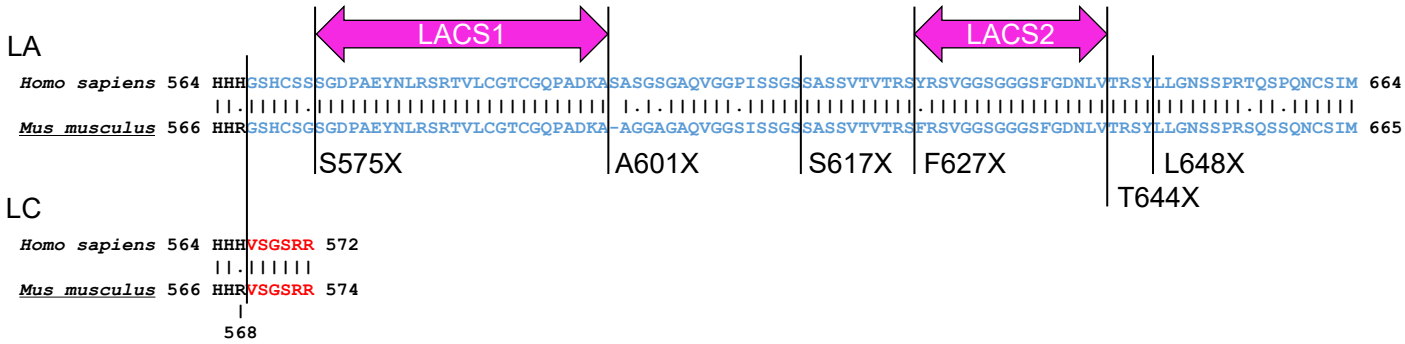
LA
LACS1
LACS2
Homo sapiens 564 HHHGSHCSSSGDPAEYNLRSRTVLCGTCGQPADKASASGSGAQVGGPISSGSSASSVTVTRSYRSVGGSGGGSFGDNLVTRSYLLGNSSPRTQSPQNCSIM 664
Mus musculus 566 HHRGSHCSGSGDPAEYNLRSRTVLCGTCGQPADKA-AGGAGAQVGGSISSGSSASSVTVTRSFRSVGGSGGGSFGDNLVTRSYLLGNSSPRSQSSQNCSIM 665
S575X
A601X
S617X
F627X
L648X
T644X
LC
Homo sapiens 564 HHHVSGSRR 572
Mus musculus 566 HHRVSGSRR 574
568

B

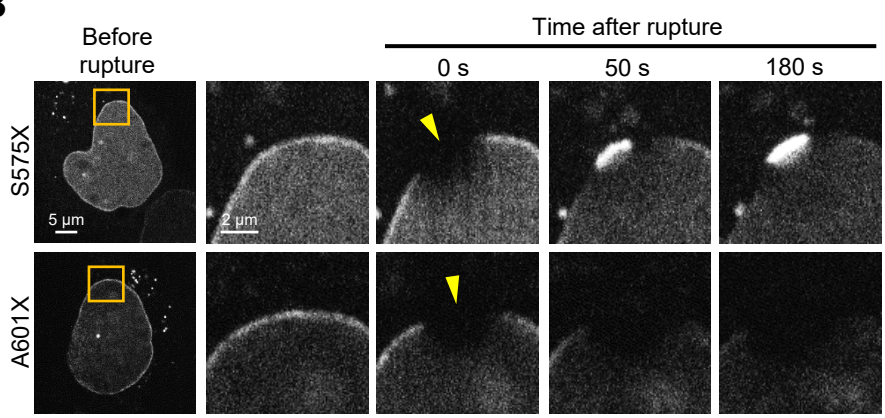
Before rupture
Time after rupture
0 s
50 s
180 s
S575X
A601X
5 µm
2 µm

C

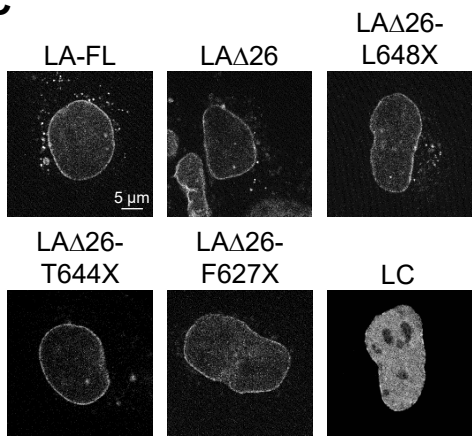
LA-FL
LAΔ26
LAΔ26-L648X
LAΔ26-T644X
LAΔ26-F627X
LC
5 µm

D

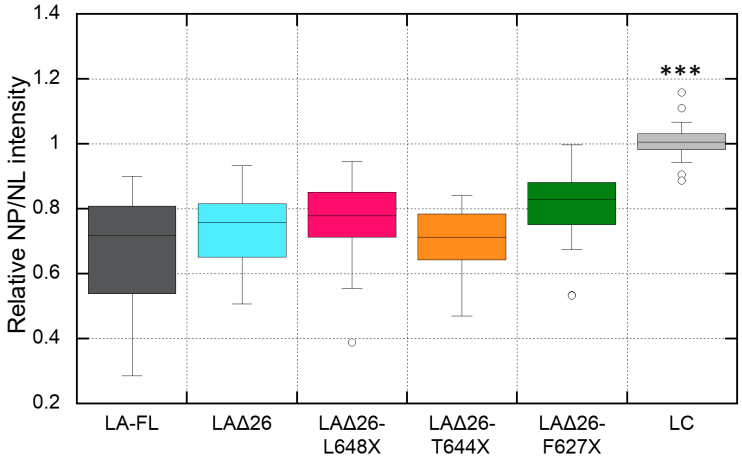
Relative NP/NL intensity
1.4
1.2
1
0.8
0.6
0.4
0.2
***
LA-FL
LAΔ26
LAΔ26-L648X
LAΔ26-T644X
LAΔ26-F627X
LC

E

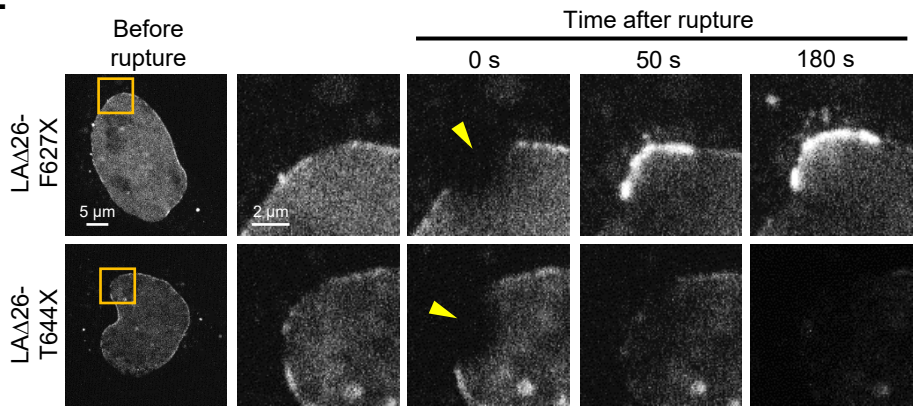
Before rupture
Time after rupture
0 s
50 s
180 s
LAΔ26-F627X
LAΔ26-T644X
5 µm
2 µm